

# High-efficiency water splitting systems

Matthias M. May\*<sup>1</sup>, Henning Döscher\*<sup>2</sup>, and John A. Turner\*<sup>3</sup>

<sup>1</sup>*University of Cambridge, Department of Chemistry, Cambridge, UK*

<sup>2</sup>*Fraunhofer ISI, Competence Center Emerging Technologies, Karlsruhe, Germany*

<sup>3</sup>*National Renewable Energy Laboratory, Golden, Colorado, USA*

\**Email: Matthias.May@physik.hu-berlin.de, Henning.Doescher@isi.fraunhofer.de, John.Turner@nrel.gov*

August 24, 2017

## Contents

<b>1</b>	<b>The need for high efficiency in solar fuel generation</b>	<b>1</b>
<b>2</b>	<b>Efficiency limitations and prospects for photoelectrochemical energy conversion</b>	<b>3</b>
2.1	Fundamental limitations: Detailed balance limit and catalysis . . . . .	3
2.2	Further relevant loss mechanisms and mitigation strategies . . . . .	6
2.2.1	Absorption by electrolyte and catalyst . . . . .	6
2.2.2	Ohmic resistivity . . . . .	7
2.2.3	Non-radiative recombination . . . . .	8
2.2.4	Energetics . . . . .	9
2.2.5	Light management . . . . .	9
2.2.6	Gas bubble management . . . . .	10
2.2.7	Multi-terminal approaches . . . . .	11
2.2.8	Concentration . . . . .	11
<b>3</b>	<b>III-V semiconductor tandem structures: A testbed for high efficiency</b>	<b>12</b>
3.1	History of the III-V compound semiconductors and high-efficiency solar cells . . . . .	12
3.2	Highly efficient III-V tandem structures in solar water splitting . . . . .	13
3.2.1	Classical III-V tandem photoelectrochemistry . . . . .	13
3.2.2	Metamorphic device concepts . . . . .	14
3.2.3	Inverted metamorphic device concepts . . . . .	16
<b>4</b>	<b>Efficiency measurement and characterization strategies</b>	<b>23</b>
4.1	Standard solar irradiance vs. laboratory light sources . . . . .	23

4.2	Tandem device characterization: a case study on common practice vs. result validation . . . . .	25
4.3	Utilization of natural sunlight and secondary illumination errors . . . . .	28
4.4	Differential spectral responsivity . . . . .	32
4.5	Solar-to-hydrogen conversion reference laboratories . . . . .	33
<b>5</b>	<b>Summary &amp; Outlook</b>	<b>34</b>

## Abstract

In this chapter, we discuss the prerequisites for high-efficiency water splitting and their implementation with tandem cells based on absorbers of the III-V semiconductor material class. A brief outline of efficiency-limiting factors shows that at a given set of boundary conditions, such as catalyst performance, the optimum tandem absorbers require a very precise control of opto-electronic properties, as facilitated by the III-V compounds. After a short history of high-efficiency solar energy conversion, we present recent implementations of highly efficient water splitting systems with solar-to-hydrogen efficiencies of 14-16% together with an outlook on further improvements. Even if other absorber systems turn out to be more cost-competitive, the III-V systems currently serve as a testbed for high-efficiency water splitting in general, with lessons to be learned for catalyst requirements, cell design, and efficiency validation. We conclude by a discussion of appropriate efficiency benchmarking routines, outlining potential pitfalls for multi-junction absorbers and how to avoid them.

# 1 The need for high efficiency in solar fuel generation

The direct photolysis of water for hydrogen production has been deemed a Holy Grail of Chemistry.<sup>1</sup> First shown in 1972 with TiO<sub>2</sub>, the photoelectrochemical splitting of water has been a dream through the decades. While the process seems to be the simplest and most straightforward approach for solar-driven water splitting, ultimately though there has not been a large-scale demonstration of a photoelectrochemical water splitting system.

For a commercially viable system, the key parameters are solar-to-hydrogen (STH) efficiency, system cost and lifetime, of which the efficiency carries the greatest weight.<sup>2</sup> This is not unexpected, since land area must be covered and that relates directly to the capital cost of the system. Unfortunately, the main focus of research over the decades has been on oxides due to their expected low cost and stability. In general oxide semiconductor have very poor solid-state characteristics,<sup>3</sup> thus their STH efficiencies remain very low.

While the number of systems, for which spontaneous solar water splitting was demonstrated, steadily increases, the range of reported efficiencies varies greatly with very few having the efficiency necessary to be considered for a viable system. As we will focus on high efficiency systems in the following, we must discuss the definition of high efficiency and motivate the permanent struggle of the solar energy communities towards this end. Solar conversion efficiencies determine a system's production rate and, at a given capital cost, its economic feasibility. If the relation between costs for the solar absorber to the cumulated cost for module, installation and land shifts away from the absorber, efficiency becomes a key factor in determining the costs per produced energy unit. In the mature market of photovoltaic solar energy conversion, such a trend can already be observed. In solar water splitting, the overall system is more complex due to gas handling facilities and consequently, these systems will be more sensitive to the impact of conversion efficiency and thus the final price of the produced hydrogen.<sup>2</sup> But how to define high efficiency? One can define this via the ratio of realised to achievable efficiency for a) a given material system or b) the overall physical limit given by thermodynamics and the shape of the solar spectrum. The latter definition is more general and in line with commercial viability and will be employed here. Note that the threshold for 'high' will increase with time as technological progress and economic demands shift the realised efficiencies towards the physical limit.

Physical efficiency limitations vary with the type of system that is used for solar water splitting. In general, one can distinguish two main approaches: PV-electrolysis systems and more tightly integrated photoelectrochemical systems. In the former approach, a dark electrolyser is driven by the output of a photovoltaic solar cell. Such a system may exhibit only electric coupling<sup>4</sup> or also mechanical coupling.<sup>5</sup> For maximum efficiency, the current-voltage behaviour of the solar cell and electrolyser must be matched whether directly coupled or interfaced with DC/DC converters, but apart from this restriction, the two systems can be developed independently. This advantage though must be tempered with the realization that the low capacity factor of PV (20%) results in the high-cost electrolyzers not operating full-time, and thus for a given product output, greatly increasing the capital costs of the system and the subsequent price of the produced hydrogen.

While for approaches beyond PV-electrolysis a variety of terminologies exist, they all share the challenge that the electrochemical load, the photovoltage of the absorber, and the photocurrent cannot be optimised independently, limiting obtainable efficiencies. Before we focus on the latter approach in the following, we first discuss the various taxonomies present in the literature.

A definition from an electrochemical perspective is the term *direct water splitting*, where the semiconductor is part of the solid–electrolyte junction, and in most cases also decorated with a catalyst. This gives rise to all the effects of semiconductor photoelectrochemistry with the Fermi level in the forbidden gap, in-gap surface states that can couple to the electrolyte, and accumulation (depletion) regions. In the case of a (metallic) catalyst present on the surface, the energetic landscape can become even more complicated due to triple points, where catalyst, semiconductor, and electrolyte meet. Indirect water splitting, on the other hand, involves in this definition a semiconductor–metal contact of either predominantly Schottky- or ohmic-type, followed by a metal–electrolyte contact. Here, the semiconductor is not in contact with the electrolyte, but energetically coupled to the electrolyte in an indirect manner via the Fermi level of the contacting metal. Other definitions of direct comprise the condition that the total number of junctions equals the number of charge-separating semiconductor–electrolyte junctions as opposed to buried junctions as in a photovoltaic (PV) device.<sup>6</sup> Such a definition does, however, not take into account that most semiconductors change their surface composition upon contact with the electrolyte forming either intrinsically a charge-separating solid–solid junction,<sup>7,8</sup> or experience charge-separation at the “catalyst”–absorber interface, as in the case of Co-Pi/BiVO<sub>4</sub>.<sup>9</sup>

## 2 Efficiency limitations and prospects for photoelectrochemical energy conversion

The design of highly efficient water splitting devices requires careful, simultaneous consideration of all efficiency-limiting factors. They comprise effects from thermodynamics, catalysis, electronic structure, materials science, and chemical engineering. Many of these challenges cannot be addressed independently, which adds to the complexity of device design. For a given set of boundary conditions such as catalyst performance, water layer thickness or solution resistivity, the optimum efficiency tandem requires an infinite fine-control of absorber bandgaps and the possibility to combine two absorbers in a tandem device. Over a wide range of bandgaps, this is possible with the III-V semiconductors.<sup>10</sup>

### 2.1 Fundamental limitations: Detailed balance limit and catalysis

The first and most well-known limit for the harvesting of solar energy by water splitting originates in the shape of the solar spectrum and the ability of a semiconductor to transform radiative energy into a chemical potential difference for electrons as discussed by Shockley and Queisser.<sup>11</sup> If we consider the steps in the photoelectrochemical water splitting process: (i) light absorption, (ii) carrier generation, (iii) carrier separation and (iv) delivery to the interface, (v) electron transfer (catalysis), and (vi) product formation, we note that the first four are in the realm of solid-state physics. Thus, the solid-state semiconducting properties (the photovoltaics) are key for an efficient solar-driven water splitting process.

In the detailed-balance limit, which was developed for photovoltaics, the main factors are radiative recombination as well as thermalisation and transmission losses due to the shape of the solar spectrum in relation to the bandgap of the semiconductor. Originally discussed for single-junction solar cells, which limits efficiencies to just above 30%, the scheme can easily be extended to multi-junction absorbers,<sup>12</sup> which greatly increases obtainable efficiencies as described below. To approach the single- or multi-junction Shockley-Queisser limit, the bandgap(s) of the absorber(s) have to be adapted to the solar spectrum. As we will see later, this requirement makes III-V compound semiconductors with their flexible opto-electronic properties the hitherto best absorbers for solar energy conversion.

In monolithic multi-junction absorbers, the photovoltages of the individual subcells add up to the overall device photovoltage, while the photocurrent is limited by the subcell that absorbs the least photons, as the current is equal in the whole device. Photon management, for instance by thinning a subcell to thicknesses below its photon absorption length, is a measure to alleviate the limiting photocurrent of the subjacent absorber with a smaller bandgap. The Shockley-Queisser limit can, in principle, be overcome by multi-exciton generation, where thermalisation losses are reduced by the generation of multiple excitons per absorbed photon. While this has recently been demonstrated for a water splitting system with lead sulphide quantum dots,<sup>13</sup> the effect is up to now only observed at significant quantum efficiencies for low-dimensional systems.

The second fundamental limit is catalysis, which is in the case of solar water splitting given by the two half-reactions of hydrogen and oxygen evolution. The difference in Nernst potentials equals the Gibb's free energy per electron and is the extractable energy by the combustion of hydrogen in a fuel cell. It can be considered the electrochemical load<sup>14</sup> – the equivalent of the energy per electron at the operating voltage of a photovoltaic cell – and depends on the type of solar fuel (1.23 eV for water splitting). We will employ the Gibb's free energy for the efficiency

definition in the following, but it should be noted that some communities also use the higher heating value, which is 1.48 eV for water splitting, for the definition of the solar-to-hydrogen efficiency.<sup>5</sup>

The fixation of the electrochemical load in solar water splitting to 1.23 eV severely limits obtainable efficiencies: In photovoltaics, an increase of the number of absorbers decreases the photocurrent by distributing the photocurrent over more subcells, but this effect is overcompensated by an increase in operating voltage and an extension of spectral sensitivity to the infrared. Consequently, more – adequately designed – junctions benefit overall efficiency. For solar water splitting, on the other hand, a reduced photocurrent of triple- or higher-order multi-junctions combined with a fixed electrochemical load reduces the efficiency and makes already double-junction cells the optimum for water splitting. An increase of the electrochemical load to higher values, however, for instance by choice of formic acid as a product of CO<sub>2</sub> reduction (1.43 eV), is equivalent to an increase of the operating voltage of a photovoltaic cell. This benefits the maximum efficiencies and renders triple cells for the production of fuels with a Gibb’s free energy beyond 1.6 eV more attractive than double junctions as depicted in Figure 1.<sup>15</sup> It shows maximum obtainable solar-to-fuel efficiencies (STF) for single, double and triple absorbers with only the fundamental limits of detailed balance and catalysis considered. The top cell(s) were thinned to maximise current matching and we see that the highest efficiencies are obtained for triple junctions in the range of 2-3 eV electrochemical load. An unknown parameter here is, however, the catalytic overpotential for a given product, which depends on the actual electrochemical reaction and its charge-transfer type. For Figure 1, the catalyst characteristics (i.e. exchange current density and Tafel slope) of IrO<sub>2</sub> for OER, which is the dominating factor in water splitting, have been employed. Other products, however, will most likely induce higher losses from catalysis.

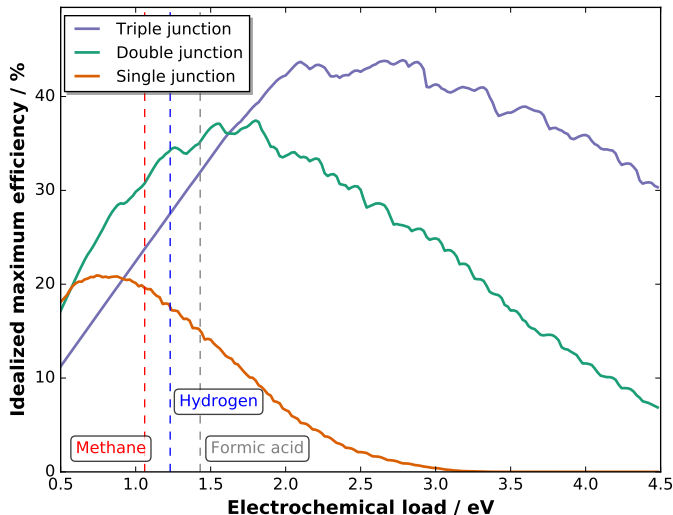


Figure 1: Ideal solar-to-fuel efficiencies in the detailed balance limit, with the Tafel behaviour of IrO<sub>2</sub> as OER catalyst. No further losses are considered; calculated with YaSoFo.<sup>15</sup>

Catalytic overpotentials increase the required voltage to initiate the reaction as a function of the current density and can typically be described by the Tafel equation, a logarithmic

voltage-current relationship.<sup>16</sup> In the case of water splitting, the overall catalytic overpotential is dominated by the multi-electron transfer oxygen evolution reaction (OER) and amounts – depending on the performance of the catalysts – to at least 300 mV at 10 mA/cm<sup>2</sup>. This limit is dictated by thermodynamics and is unlikely to be overcome.<sup>17</sup> High-performance catalysts, especially for OER in acid, often show the drawback that they are based on noble metals.<sup>18</sup> The overpotentials of hitherto known catalysts for other reactions such as CO<sub>2</sub> reduction are significantly higher: For a recent high-efficiency system with  $\eta \sim 13\%$  STF, the overpotentials of cathode and anode were almost equal and amounted to more than 800 mV.<sup>19</sup> If CO<sub>2</sub> reduction is at all viable for solar fuel production can, however, be questioned.<sup>20</sup>

Figure 2(a) shows water splitting efficiencies with an ideal tandem absorber in the detailed-balance limit with 2 mm water layer and 2  $\Omega$  ohmic drop as a function of catalyst performance. For the sake of simplicity, we assume here that the overpotential is dominated by a single catalyst described by exchange current density and Tafel slope (which are, however, not fully independent). High-performance catalysts such as RuO<sub>2</sub> are found towards the bottom left of the graph, where theoretical efficiencies approach 30% STF. Noble-metal free catalysts typically benefit from a higher earth abundance, but they often exhibit a higher Tafel slope towards 100 mV per decade and lower exchange current densities, corresponding to a shift towards the top right of the graph. This quickly decreases maximum obtainable efficiencies to values below 20% STF. The efficiencies were obtained by optimising the bandgaps of the tandem absorber (with optimum thinning) at each combination of exchange current density and Tafel slope. Again, we observe that a change in the performance of an outer parameter requires an adjustment of the bandgaps of the absorbers. This is illustrated in Fig. 2(b), where the resulting sum of the bandgaps for the ideal two-junction tandem absorbers is shown. With a decreasing catalyst performance, the photovoltage generated by the absorber must increase to compensate for the higher overpotentials. This is accomplished by increasing the bandgaps, which leads to a reduction of the photocurrent and therefore efficiency.

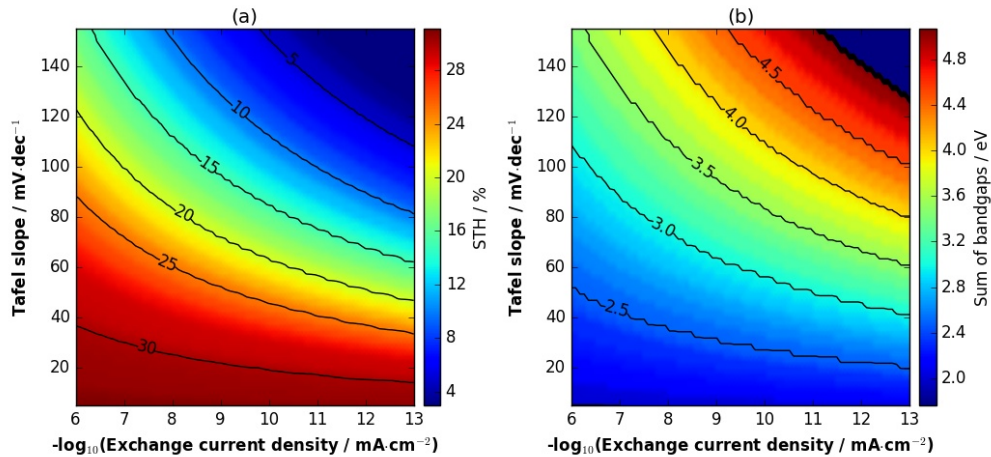


Figure 2: Ideal water splitting efficiencies (a) for a dual-junction tandem as a function of Tafel slope and exchange current density in the detailed balance limit as a function of catalyst performance, with 2 mm water layer and 2  $\Omega$  ohmic drop. (b) The sum of the bandgaps for the optimum tandem absorber.

The above mentioned two fundamental limits are by far the most important boundary con-

ditions for high-efficiency water splitting. The minimum photovoltage dictated by electrochemistry requires absorbers with suitable bandgaps and material properties. If the delivered photovoltage is too low to drive the reaction, the efficiency is zero. Absorbers in the intermediate bandgap range of ca. 1.2-1.4 eV might deliver high photocurrents,<sup>21</sup> but if the achieved photovoltages are in the order of only 500 mV or below, this is insufficient for water splitting. Equally, materials with high photovoltage, but high bandgap, such as TiO<sub>2</sub>, fail because of low photocurrents due to a lack of UV photons in the solar spectrum. Multi-junction devices with adequate bandgaps are therefore imperative for efficient photoelectrochemical water splitting.

## 2.2 Further relevant loss mechanisms and mitigation strategies

In addition to the fundamental limits, which constitute significant restrictions for solar fuel efficiencies, there are further loss mechanisms which can, in principle, be minimised. Losses such as ohmic resistivities and light absorption by the electrolyte depend on absorber materials and cell design. These are to some extent unavoidable and their magnitude depends on the characteristics of the design, such as the distance between the active areas of the half-cell reactions. Mitigation requires specific optimisation not only of the photoelectrochemical cell, but also of the absorber, which will be discussed in the following.

### 2.2.1 Absorption by electrolyte and catalyst

An electrolyte layer in front of the cell acts as a spectral filter, which cuts the photon flux mainly in the infrared.<sup>22-24</sup> As water splitting takes place in an aqueous electrolyte, this effect could also be considered one of the more fundamental limits. Its impact, however, depends on the cell design and the bandgap of the bottom cell absorber. In cases, where cell engineering cannot be driven further, the absorbers must be adapted, for instance to alleviate current limitation by the bottom cell. Finally, the absorption of light by the catalysts, which can affect photocurrents over a wide spectral range, has to be reduced, which is achieved for instance by the tailoring of size and distribution of catalyst nanoparticles.<sup>15,25</sup> However, depending on the catalytic properties of the bare semiconductor, co-catalysts might not be needed at all.

The effect of a water layer (Fig. 3b), on the efficiency and thus the bandgaps, leads to a reduction of obtainable maximum efficiencies with an increasing thickness of the water layer. The optimum bandgaps of the subcells, however, show a non-linear behaviour: In the limit of very thin water layers, the bottom cell bandgap must be decreased to provide more current, which has to be counter-balanced by an increase of the top cell bandgap to still provide enough photovoltage. The latter measure also reduces current limitation by the bottom cell. Around 0.3 cm thickness, however, the infrared fraction of the solar spectrum is attenuated to an extent, where a further decrease of the bottom cell bandgap does not benefit its photocurrent, which is why the optimum bandgap suddenly increases to about 0.9 eV. Current matching can still be maintained by thinning of the top cell, where the bandgap can now be reduced again with the bottom cell generating more photovoltage. Beyond 1.5 cm of water, the absorption also starts to affect the visible range, decreasing the photocurrent of the top cell. The optimum bandgap of the top cell is therefore further reduced. The loss in photovoltage is partly compensated by an increase of the bottom cell bandgap, partly by the reduced catalytic overpotential at the overall lower current density.

In the case of the metamorphic tandem discussed in section 3.2.2 below, where the bottom cell absorber bandgap is larger than the optimum, a water layer thickness of 2 mm – technically

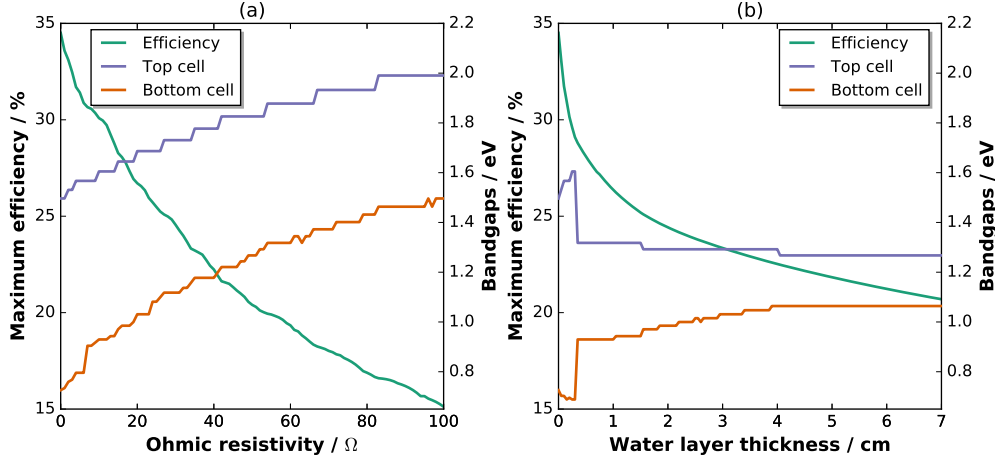


Figure 3: Maximum solar-to-hydrogen efficiencies and the corresponding optimum bandgaps for double junction absorbers in the detailed balance limit with additional losses: (a) ohmic drop and (b) absorption (data from Ref.<sup>26</sup>) by liquid water.

certainly feasible – reduces the current by only  $0.1 \text{ mAcm}^{-2}$ . In the popular combination  $\text{BiVO}_4$  (2.4 eV bandgap) with Si (1.12 eV) on the other hand, the top cell is strongly current limiting and it takes 4 cm of water for the current to drop by ca.  $0.1 \text{ mAcm}^{-2}$ . For higher-order multi-junction devices such as triple junction cells, where the bottom absorber has a bandgap deeper in the infrared, the limiting impact of a water layer is, however, even more pronounced than in the double-junction case. While for high-efficiency water-splitting, triple-junctions are of limited interest, other solar fuel pathways (in an aqueous electrolyte) with higher electrochemical load could require the high photovoltage of a triple-junction and will therefore suffer more from the infrared absorption of water.

While thin water layers in front of the absorber reduce the absorption, they increase the overpotential from ion transport in the solution. The size of gas bubbles – which can be reduced by surfactants to some extent – creates another boundary condition for the thickness of the water layer. An embedding of counter-electrode and gas-conduction channels in the front window, similar to the contact fingers in photovoltaics, could potentially reduce these effects.<sup>15</sup>

There are two important messages from these observations for the design of efficient water splitting devices: Devices should be benchmarked under realistic conditions (see Section 4), as a variation of parameters such as ohmic drop or parasitic absorption by electrolyte and catalyst can significantly change optimum bandgap combinations and potentially require new absorber materials. Furthermore, the adaptation to the working conditions of a solar water splitting device necessitates a precise fine-tuning of opto-electronic properties such as bandgaps and absorber thickness, as is feasible with the III-V semiconductors.<sup>10</sup>

### 2.2.2 Ohmic resistivity

Ohmic resistivities that stem from the ionic conductivity of the electrolyte, a membrane or from within the solar cell effectively increase the overvoltage required to drive the reaction.<sup>27,28</sup> Unlike the Tafel behaviour of the overpotential from catalysis, these resistivities show a linear

increase of the overpotential with current.

While the reduction of solid-state ohmic drops, for instance from the ohmic back-contact between semiconductor and counter-electrode, is greatly reduced by the use of the appropriate contact fabrication technology,<sup>29</sup> the ion transport resistivity in the electrolyte can be reduced by advanced electrode geometries such as supertube arrays or flow reactors.<sup>15,30</sup> If ohmic drops remain high due to cell design or the use of low-conductivity electrolytes, the bandgaps of the absorbers have to be increased to provide sufficient photovoltage: Figure 3(a) shows maximum efficiencies for solar water splitting in the detailed balance limit (as Fig. 1), with the introduction of an ohmic resistivity from solar cell and/or electrolyte. This loss mechanism causes a steep decrease of the obtainable efficiencies, with a drop to about half of the initial efficiency at  $60\ \Omega$ . To provide enough photovoltage for the effectively increased overpotential, both subcells have to increase their bandgap.

Shunt resistances in the device have to be considered as a loss mechanism as well.<sup>31,32</sup> While the typical origin of shunt resistance in solid-state devices, the conduction along grain boundaries, can be considered negligible in high-quality epitaxial III-V solar cells, the processing of samples, especially if the sample area is very small, can reintroduce them. In addition to solid-state shunt resistances, Seitz et al.<sup>31</sup> argue that charge-transfer from the semiconductor to the electrolyte can also be an origin of a shunt resistance, effectively decreasing obtainable efficiencies.

### 2.2.3 Non-radiative recombination

Non-radiative recombination, which originates for instance at growth-induced defects in the semiconductor,<sup>33,34</sup> are a challenge for materials science and can be minimised by adequate absorber growth or the use of nanostructures. For some materials, however, high recombination rates appear to be an intrinsic property of the material, such as in the in principle very attractive dilute III-V nitrides.<sup>35,36</sup> For the classical III-V semiconductors, radiative recombination was greatly reduced over time by advances in epitaxial growth and the development of surface and interface passivation layers, see also Section 3.1. It can, however, become an issue for heteroepitaxy of compounds with a large lattice-mismatch or when growing polar III-V's on non-polar substrates. The former challenge can be tackled by metamorphic or inverted metamorphic growth concepts (Sec. 3.2.2&3.2.3) or wafer bonding, where two wafers are brought in contact after surface sputtering in vacuum, forming covalent bonds with defects confined to a few atomic layers.<sup>37</sup> Recent efforts regarding the latter are directed towards defect minimisation of III-V heteroepitaxy on Si.<sup>37-39</sup>

Surface charge-carrier recombination in solar water splitting systems is still an issue, often reducing the photovoltage of a device working in photoelectrochemical mode compared to the voltage obtained for the same absorbers in photovoltaic mode. For InP, charge trapping states related to certain oxygen motifs on the surface were predicted by Wood et al.<sup>40</sup> Comparing water and oxygen absorption on clean InP surfaces, it was found that these states originate in oxidation by molecular oxygen, but can be largely avoided by water, forming a different surface oxide species.<sup>41</sup> This was later also confirmed for GaInP by ambient-pressure photoluminescence experiments.<sup>42</sup> Here, a challenge for high-efficiency III-V water splitting systems remains to develop electronic surface passivation layers that are simultaneously stable in the electrolyte, reduce surface charge-carrier recombination and feature a suitable coupling to the electrocatalyst. Phosphates partially fulfil these requirements, but, at this current stage of development, lack long-term stability in the electrolyte.<sup>43</sup>

### 2.2.4 Energetics

Unfavourable energetic alignment of hetero-junctions within the absorber and at the interface to catalyst or electrolyte are a property of the electronic structure of a material or its (oxidized) surface and leads to photovoltage losses. For p-GaP, this photovoltage loss amounts to about 800 mV due to a conduction band offset between GaP and its oxide formed upon contact with the aqueous electrolyte.<sup>8</sup> In the case of the catalyst–semiconductor interface, such losses can in some cases be mitigated by using pinch-off effects at the interface of highly doped semiconductors with catalyst nanoparticles, or surface transformations that lead to a more suitable energetic alignment than the directly oxidised surface.<sup>43,44</sup> Also adequate doping profiles allow, to some extent, for a control of internal band alignment, as well as the energetics between semiconductor and electrolyte.<sup>45</sup> For efficient tunnel junctions between subcells, doping profiles have to be as abrupt as possible. The abruptness can be improved by the selection of an appropriate (i.e. III-rich or V-rich) surface termination before switching to the next stoichiometry during growth.<sup>7,46</sup> As the theoretical description of III-V semiconductors is well established, the framework of density functional theory becomes predictive regarding energetics and charge-trapping states,<sup>40,47,48</sup> which promotes fundamental understanding and device design.

### 2.2.5 Light management

Photon management describes approaches to maximise the overall conversion from impinging photons to current. The main factors here are a minimisation of reflection and transmission losses and the adaptation of the absorber’s thickness by thinning. Yet also the refractive indices of the surrounding medium is a parameter that finally impacts the open-circuit voltage as analysed in detail by Létay and Bett for single-junction concentrating solar cells.<sup>49</sup> (In the calculations presented here, we used their idealised assumption of a mirror at the back and an interface to air at the front.) The effect has recently been described as external radiative efficiency<sup>50</sup> and also has to be considered for solar water splitting applications,<sup>32</sup> especially as the surrounding medium of the top absorber is not air, but water.

To reduce reflection losses, anti-reflection coatings (ARC) such as TiO<sub>2</sub> combined with MgF<sub>2</sub> are widely used in photovoltaics. In solar water splitting, the optical interface is typically comprised of an outer cell with a transparent window, a thin layer of water, a catalyst and/or protection layer followed by the absorber. Reflective losses at the quartz-window of the outer cell to air amount to ca. 4% of the incident light.<sup>23</sup> Therefore, an ARC has to be applied to both, the outer cell window and the surface of the absorber. Ideally, anti-reflective properties can be achieved by the protection layer or the catalyst. Nanoparticles have been demonstrated to serve this purpose to some extent, reducing the reflection in the water layer, but not necessarily in air due to their different refractive indices.<sup>15</sup>

The above mentioned fundamental efficiency limitation imposed by the solar spectrum and absorption threshold of the semiconductors severely restricts the choice of absorber bandgaps and therefore the materials. This condition can, however, be partially weakened by photon management in the form of thinning: Here, the top absorber(s) of the multi-junction cell is thinned below the absorption length to partially transmit photons above its bandgap to the subsequent absorber. Such an approach can be necessary if for instance lattice matching in an epitaxial absorber restricts feasible lattice parameters and therefore stoichiometry and bandgap. It was also used for a recent metamorphic water splitting tandem absorber.<sup>43</sup> Fig-

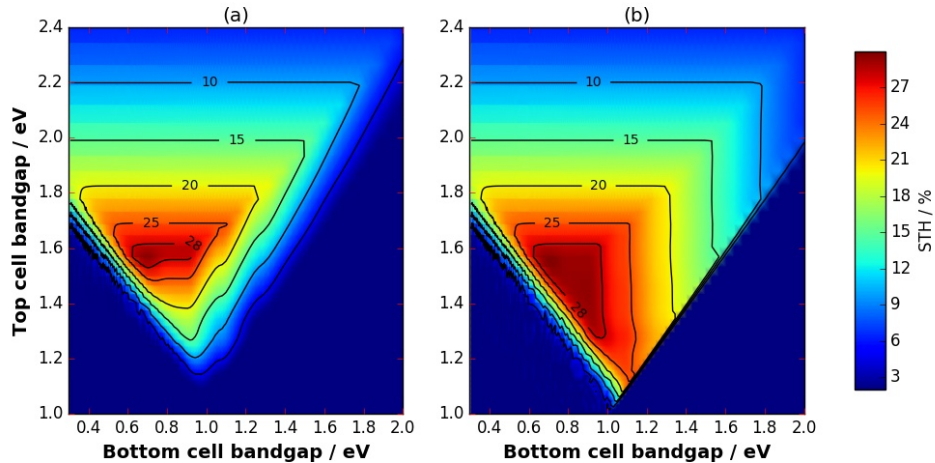


Figure 4: Maximum STH efficiencies of a dual junction in the detailed-balance limit with 2 mm water layer,  $2\Omega$  ohmic drop, and  $\text{IrO}_2$  as a catalyst. (a) No thinning, (b) with optimum thinning of the top absorber.

Figure 4 plots theoretical STH efficiencies as a function of top and bottom cell bandgaps. The comparison of Fig. 4(a), where no thinning was allowed, with Fig. 4(b) shows that the region of high efficiencies beyond 20% STH in Fig. 4(b) is significantly broadened. In the latter case, optimum thinning was assumed, demonstrating that it greatly extends the range of attractive bandgap combinations.

### 2.2.6 Gas bubble management

Especially for high-efficiency systems with their high photocurrents and corresponding gas production rates, the formation of gas bubbles becomes a challenge. They will scatter light and reduce the photon flux on the sample, while gas bubbles sticking to the surface reduce the reactive area.<sup>51</sup> The latter factor can be reduced by designing the surface to be hydrophilic. Another effect is mechanical and chemical stress, which was already noted in early high-efficiency systems, where corrosion appeared to be accelerated in areas, where bubble accumulation occurred.<sup>52</sup> This can be partially compensated by the use of surfactants, yet some surfactants such as Triton X can also act as reactants: A 1 M  $\text{HClO}_4$  solution with 5 mM Triton X develops a yellowish colouring after several hours of water splitting using only Pt electrodes, which indicates that the Faradaic efficiency for water splitting in the solution is less than unity, which can also deteriorate efficiency measurements.

The direction of bubble protrusion is given by gravity, which can render the orientation of the cell, i.e. horizontal versus upright, a factor for both stability and efficiency. As already noted by Khaselev and Turner,<sup>52</sup> a typical, not fully upright solar cell orientation will ease bubble detachment from the surface and consequently reduce mechanical stress. This will, however, change the angle between photon and bubble path, lengthen the light path subject to scattering (as well as absorption by the electrolyte) and finally reduce efficiency. In concentrating systems, where the position of the sun is followed by means of a tracker, the tilt and therefore the magnitude of this effect will vary over the course of a day. As a consequence, gas bubble management has to be part of high-efficiency cell design, but also has to be considered for

efficiency evaluation. A precise quantification of the effect on obtainable efficiencies does, however, remain elusive.

### 2.2.7 Multi-terminal approaches

In conventional, monolithic multi-junction devices, the current is collected at two contacts at the front and back of the device, for photovoltaic operation at an ohmic solid–solid contact, for photoelectrochemical operation at a solid–liquid contact. This approach has the effect that the current is constant in the whole device and voltages add up. In multi-terminal approaches, these two restrictions are relaxed by the introduction of additional contacts in between the subcells to collect the current. This approach indeed enables high efficiencies in photovoltaics, as for instance the current limitation by the popular Ge substrate, also used as bottom cell in a four-junction device, is lifted.<sup>53</sup> While it could, in principle, also be used in photoelectrochemical devices, for instance by harvesting surplus voltage in the form of electrical power in a hybrid device, this would remove the advantage of the simplicity of an integrated water splitting system.<sup>54</sup>

### 2.2.8 Concentration

Light concentration up to 1000 suns is routinely used in high-efficiency photovoltaics, as it not only shifts the electricity generation costs away from the absorber to the overall system, which benefits pricey absorber materials, but also improves the total efficiency: The open-circuit voltage of a cell increases logarithmically with the light intensity and so does, to a lesser extent, the fill factor. At very high concentrations, charge transport becomes an issue, which is why most concentrating photovoltaic cells show a global maximum of efficiency at concentrations in the order of 200–500 suns. The requirement of direct sunlight not impeded by clouds does, however, restrict the application case for concentrating solar cells geographically.

Also in solar water splitting, light concentration was already used in the classical GaInP/GaAs tandem (ca. 10 suns power equivalent).<sup>52</sup> Due to the benefits for expensive absorbers, such an application is considered the commercial case for III-V absorbers in economic models, with a very high sensitivity of the hydrogen price on the system efficiency.<sup>2</sup>

### 3 III-V semiconductor tandem structures: A testbed for high efficiency

The reason for the widespread use of III-V semiconductors in electronic devices such as light-emitting diodes, sensors, and solar cells are their highly flexible opto-electronic properties. The magnitude as well as the direct/indirect nature of their bandgap can be tuned over a wide range by combining several elements of group III and V to form binary, ternary or quaternary compounds.<sup>10</sup> The flexibility also holds true for the energetic positions of valence band maximum and conduction band minimum, which determines the band offset of heterojunctions, an important parameter for the design of quantum wells or tunnel junctions.

As III-V semiconductors enable absorbers providing high photovoltages at high photocurrents, photovoltaic or photoelectrochemical devices based on this material class have become a testbed for high efficiencies: Single factors such as ohmic resistivity, parasitic light absorption, bubble management or the energetics of semiconductor–catalyst junctions have to be carefully addressed. Lessons learned from the design of these systems will also benefit materials that are currently not as mature, but might show a higher potential for scalability due to lower material or production costs.

#### 3.1 History of the III-V compound semiconductors and high-efficiency solar cells

Earliest studies on solar cells based on the III-V material class date back to 1954,<sup>55</sup> the same year silicon solar cells could already demonstrate 6% conversion efficiency.<sup>56</sup> Only one year later, Gremmelmaier reported 4% efficiency for a single-junction GaAs photovoltaic cell, albeit on a very small area and suffering from a – in comparison to Si – lower available material quality.<sup>57</sup> The potential of binary III-V semiconductors covering a wide range of bandgaps to exploit the solar spectrum more efficiently than Si-based solar cells was quickly discovered,<sup>58</sup> yet bulk material quality as well as surface charge carrier recombination were still an obstacle. The latter was tackled by Alferov et al. in 1970, developing the first III-V heterojunction solar cell, where they terminated the GaAs with an  $\text{Al}_x\text{Ga}_{1-x}\text{As}$  layer.<sup>59</sup> It took another five years until the first concentrating GaAs solar cells equipped with an  $\text{Al}_x\text{Ga}_{1-x}\text{As}$  window layer surpassed with about 23% reported efficiency at 10 suns the efficiency of Si solar cell technology.<sup>160</sup> In the same year, III-V semiconductors appeared for the first time in the context of solar water splitting, when Yoneyama et al. proposed the use of a p-GaP photocathode in combination with a  $\text{TiO}_2$  photoanode for unassisted water splitting.<sup>61</sup> Due to the high bandgap of the  $\text{TiO}_2$  absorber, however, already the theoretical limit of this wired multi-junction approach was intrinsically limited to below 2%. A few years later, the first photovoltaic III-V tandem cells were developed which provided an open-circuit voltage of 2 V and would therefore in principle have already afforded unbiased water splitting.<sup>62</sup>

One of the main driving factors for the further development of III-V multi-junction cells was – and still is – high-efficiency photovoltaics in space applications, where the material cost is less relevant. While this potential had been recognised quite early, the heavy weight of GaAs solar cells based on GaAs wafer substrates did, however, initially outweigh the efficiency benefits of III-V solar cells in space.<sup>63</sup> It took until the 1990s for thin-film III-V solar cells to be deployed as power supply in satellites.<sup>64</sup> Advances in metal-organic vapour phase epitaxy, the preparation technique that started to replace liquid phase epitaxy in the 1980s, are nowadays

---

<sup>1</sup>It has to be noted, however, that photovoltaic efficiency reports up to the mid/end of the 1970s are prone to relatively large errors due to non-standardised benchmarking routines.

routinely enabling efficiencies of triple-junction solar cells for space beyond 30%.<sup>65</sup> These cells are at the moment mostly based on epitaxial thin films grown monolithically on a Ge substrate. The latter acts as the bottom cell and has the advantage of reduced weight and cost compared to GaAs wafers. Recent trends here replace the Ge with the more abundant and less expensive Si,<sup>37</sup> targeting the contribution of substrates to III-V PV cell manufacturing costs, presently amounting to more than 50%.<sup>66</sup>

Reaching maturity in space, high-efficiency photovoltaics came back to earth in the form of terrestrial concentrator photovoltaics, where the higher sensitivity of the market to materials cost is (partially) compensated by the use of a light concentrating element with a small-area absorber. Here, wafer-bonded quadruple junction cells currently enable efficiencies of 46%,<sup>67</sup> and multi-junction cells of higher order will soon break the 50% mark.

Still lacking a commercial application case, the further development of III-V-driven water splitting was progressing in a comparatively abrupt, non-evolutionary manner. Already in the 1980s, InP photocathodes were demonstrated to be relatively stable and efficient, but only with applied bias due to the low bandgap of InP resulting in a low photovoltage.<sup>68</sup> The first breakthrough for highly-efficient, immersed water splitting came in 1998, when a GaInP/GaAs cell with one buried and one solid—liquid junction, developed at NREL, enabled 12.4% unbiased water splitting under concentrated illumination, a record, which was to remain unchallenged for 17 years.<sup>52</sup> The first full device equipped with a gas-separating membrane, designed at JCAP, employed a commercial GaInP/GaAs photovoltaic tandem from AZUR Space equipped with a TiO<sub>2</sub> protection layer and enabled 10% efficiency.<sup>69</sup> A further step towards the 15% STH efficiency milestone was achieved by a photovoltaic double-junction GaInP/GaInAs core, grown metamorphically on a Ge substrate. Here, photoelectrochemical in situ functionalisation provided (electro)chemical and electronic passivation of the immersed surface that was decorated with Rh electrocatalyst nanoparticles leading to 14% STH efficiency under one sun.<sup>43</sup> Less than two years later, the highest STH efficiency benchmark is now 16%, continuing the trend to adopt buried charge-separating junctions, here with an inverted metamorphic GaInP/GaInAs tandem, completed by a sputtered PtRu co-catalyst layer.<sup>45</sup> Up to now, however, all of these systems suffer from a limited stability in the order of 10-100 hrs.

For non-immersed systems, where typically a double- or triple junction photovoltaic absorber is coupled to a single electrolyser or an array thereof, 16 and 18% STH efficiency under one sun were already reported in 2001.<sup>70,71</sup> The current benchmarks here are III-V concentrator photovoltaic cells, that are with around 30% STH efficiency under 40-200 suns about twice as efficient as the immersed systems.<sup>5,72</sup>

## 3.2 Highly efficient III–V tandem structures in solar water splitting

### 3.2.1 Classical III–V tandem photoelectrochemistry

As high efficiency solar converters are necessary for efficient photoelectrochemical water splitting it follows that III-Vs would be excellent candidates for water splitting devices. The first reported use of a III-V for water splitting was a tandem consisting of a p-GaP photocathode and a n-TiO<sub>2</sub> photoanode with a reported water splitting efficiency of 0.25%<sup>73</sup>. Later a separated tandem of p-InP as the photocathode and n-GaAs as the photoanode was used and a water splitting efficiency of 8% was reported<sup>74</sup>. However, these devices utilized two simultaneously illuminated semiconductors, thus each of their electrodes operated separately. This is not an ideal configuration as the maximum possible efficiency cannot be reach with this design.

In 1994<sup>75</sup>, NREL described the first monolithic III-V tandem solar cell consisting of a lattice-matched GaInP<sub>2</sub>/GaAs p/n, p/n tandem cell. Based on that design, in 1998 the monolithic photoelectrochemical (PEC)/PV device was developed with a p-GaInP<sub>2</sub> photoelectrochemical top cell, backed by a p/n GaAs cell. A water splitting efficiency of 12.4% was reported.<sup>52</sup>

### 3.2.2 Metamorphic device concepts

Lattice-matched epitaxial growth, where the lattice constant of the epitaxial layer matches the substrate, avoids growth defects originating in relaxation of the top absorber. This restriction to a lattice constant does, however, limit the material choice as ternary or quaternary III-V compounds exhibit stoichiometry-dependent lattice constants with associated bandgaps. The boundary condition can, however, be relaxed by metamorphic growth, where the lattice constant is changed stepwise from the substrate to the subsequent absorber in so-called grading layers. Defects do still arise, but they are limited to dedicated layers with a thickness in the order of 1  $\mu\text{m}$  that are not part of the photoactive region.<sup>76</sup> The cells above the grading layer as well as the window layer are then typically lattice-matched.

With such a metamorphic photovoltaic tandem core, based on GaInP (bandgap: 1.78 eV) and GaInAs (1.26 eV) grown pseudomorphically on a Ge substrate, photoelectrochemical in situ modification recently enabled 14% STH.<sup>43</sup> This value was later, in addition to the efficiency measurements at Helmholtz-Zentrum Berlin, confirmed for a different sample at the benchmarking facilities of JCAP.

Here, the highly n-doped AlInP window layer, that terminated the GaInP top cell, served as the starting point for further surface treatment. After photoelectrochemical etching, it was functionalised in a single aqueous RhCl<sub>3</sub> solution to avoid unfavourable<sup>41</sup> exposure of the III-V surface to ambient oxygen. A pulsed, stroboscopic photoelectrochemical deposition of Rh nanoparticles simultaneously provided the HER electrocatalyst and formed a phosphate-rich surface, which appears to passivate the surface both electronically and (electro)chemically. The resulting device structure is sketched in Figure 5.

Originally intended for concentrating photovoltaic operation, the device was optimized to AM 1.5D illumination, with a thinning of the GaInP top cell to alleviate the current-limitation by the bottom cell. Theoretically, the bandgap combination of 1.78 and 1.26 eV could feature 16.9 mAcm<sup>-2</sup> without thinning and 18.5 mAcm<sup>-2</sup> with optimum thinning under AM 1.5G, equivalent to 20.8 and 22.8% STH.

Initial potentiostatic catalyst deposition adapted from previous work on InP photocathodes<sup>77</sup> induced strong catalyst absorption due to a nanoparticle morphology featuring rather large particles. A pulsed (50 ms) deposition with the addition of stroboscopic illumination improved the resulting catalyst morphology and its associated transparency, enabling saturation current densities closer to what was expected for photovoltaic operation with anti-reflection coating.<sup>43</sup> Nanoparticle sizes showed a rather wide distribution, with an average diameter of ca. 20 nm.

Fill factor and open-circuit potential were, however, below the values expected from the photovoltaic device, indicating non-ideal energetic alignment and surface charge-carrier recombination. The photocurrent for an unbiased operation under simulated AM 1.5G (Wacom WXS-50S solar simulator, vertical configuration) with a wired RuO<sub>x</sub> OER counter-electrode was 11.5 mA/cm<sup>2</sup>, the saturation current 14 mA/cm<sup>2</sup> (Fig. 7, green curve). A further decrease of the photovoltage losses associated with photoelectrochemical operation by 250 mV could unlock access to this photocurrent, which would result in 17.2% STH.

The solution for efficiency determination was 1 M perchloric acid with no surfactants and

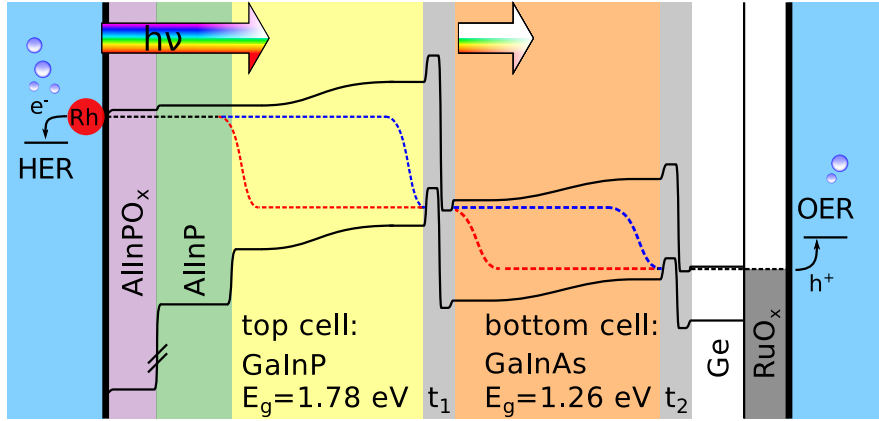


Figure 5: Energy schematic of the metamorphic tandem layer structure under illumination. The ohmic back contact is connected to a sputtered  $\text{RuO}_x$  counter electrode for the oxygen evolution reaction (OER). The hydrogen evolution (HER) takes place at the Rh nanoparticles. Contacts between subcells are facilitated by tunnel junctions, where switching between majority-charge-carrier types occurs. Black, dashed lines represent the Fermi level, blue (red) the Quasi-Fermi levels of electrons (holes) and arrows indicate the illumination. Adapted from Ref.<sup>43</sup>

sample sizes were typically around  $0.5 \text{ cm}^2$ , as defined by the black, high-viscosity Electrolube ER 2162 epoxy. Faradaic efficiency was confirmed to be (near) unity by long-term eudiometric gas collection, finding the expected gas volumes for  $\text{H}_2$  and  $\text{O}_2$  evolution. The stability of the device was, however, limited with a 50% decrease of the photocurrent over a period of 40 h. One problem here appeared to be the mechanical stress induced by the hydrogen bubbles on the catalyst nanoparticles, as a horizontal configuration showed a tendency towards higher lifetimes.

Figure 6(a) shows external quantum efficiencies (EQE) of the tandem operated in photovoltaic mode with ohmic Au front-contacts. After etching of the cap layer, the EQE of the tandem was significantly below the values of the fully processed photovoltaic device (cf. Ref.<sup>5</sup>) due to the lack of an anti-reflection coating (ARC). The deposition of a very high loading of Rh catalyst nanoparticles decreases these values even more due to the introduction of light scattering (in air) and absorption by the catalyst. The scattering in air is evidenced by an optically greyish-turbid appearance.

The former effect is, however, reversed by the introduction of a water layer on top of the surface that, with its higher refractive index, turns the catalyst layer into an ARC, partially compensating for the catalyst absorption.<sup>15,78</sup> An *in situ* measurement of reflectance in the electrolyte before and after catalyst deposition confirms these ARC properties (Fig. 6b), the reflectivity is strongly reduced. The combined effect of ARC and catalyst absorption is, however, not spectrally uniform and therefore changes the solar spectrum impinging on the absorber. An analysis of relative EQE before and after catalyst deposition suggests that the top cell becomes current-limiting, which should be compensated by a reduction of the top absorber thinning.

Recent progress in the tandem absorber epitaxy led to an increased transparency of the tunnel junctions.<sup>5</sup> This improved the efficiency of the device, which was designed for a concen-

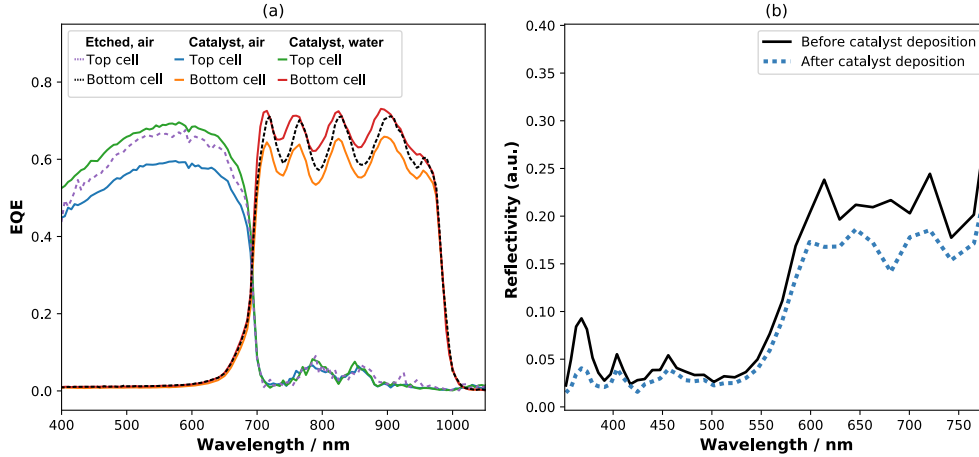


Figure 6: (a) External quantum efficiencies of the metamorphic device in photovoltaic operation at different stages of device processing. (b) Reflectance of the tandem in  $\text{RhCl}_3$  solution before and after Rh nanoparticle deposition.<sup>15</sup>

trating photovoltaic operation, i.e. a maximisation of the electric power output at AM 1.5D and not for a maximisation of the photocurrent at a certain threshold voltage as required for solar water splitting. A first step towards an absorber customised for solar water splitting at AM 1.5G comprised an adapted thinning derived from EQE measurements.<sup>15</sup> Combined with a further optimised catalyst deposition on a  $\text{TiO}_2$  protection layer, this already promises significantly efficiency improvements for this device concept.<sup>79</sup> Further enhancements of the efficiency require the improvement of surface energetics to reduce photovoltage losses as well as the reduction of surface charge-carrier recombination, which then would allow for a further reduction of absorber bandgaps to increase the photocurrent.

### 3.2.3 Inverted metamorphic device concepts

Engineering solutions such as top-absorber thinning as described above and in section 2.2.5 aim to mitigate practical STH efficiency limitations imposed by limited design flexibility with a given set of materials. In case of a too small difference in bandgap energy, i.e. between the classical GaInP (1.81 eV) and GaAs (1.42 eV) tandem absorbers, the remainder of the solar photon flux reaching the bottom junction does not nearly suffice to match the top absorber current.<sup>80</sup> Thinning represents a practical work-around for limited materials design capabilities inferior to the options of either raising the top absorber bandgap (for higher voltage at equal current) or decreasing the bottom absorber bandgap (higher current, but decreased voltage).

Figure 8 illustrates these design options based on a theoretical detailed balance contour plot (a) and the bandgap vs. lattice constant relation for III-V semiconductors (b) limiting their implementation in practice. Here, efficiencies were calculated using a water layer of 2 mm, no thinning, and a constant overpotential of 800 mV to represent losses from catalysis and ohmic drop. Note that the latter condition changes the shape of the isoefficiency contourlines when compared to Fig. 4(a). The classical GaInP/GaAs tandem features STH prospects of only 15% efficiency (black dot). Both higher voltage and about 19% efficiency would be possible on the same GaAs substrate (red line) when implemented with a higher top absorber bandgap. In

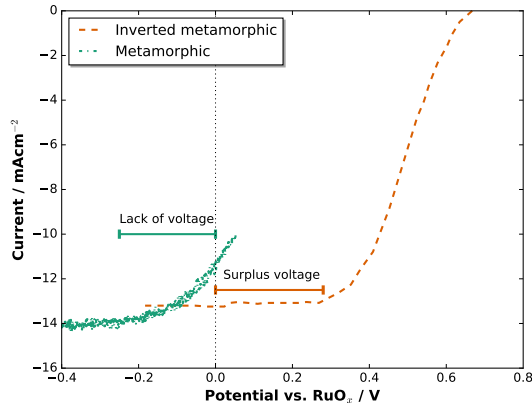


Figure 7: Comparison of the I-V curves of the metamorphic (green curve) and the inverted metamorphic (orange curve, sec. 3.2.3) tandem against a  $\text{RuO}_x$  counter-electrode.<sup>43,45</sup> While the metamorphic tandem cannot realize its full photocurrent due to a lack of photovoltage, the inverted metamorphic device generates surplus voltage, which would make the use of more earth-abundant catalysts feasible, but suffers from higher reflection losses.

practice, excessive dislocation nucleation upon reducing the lattice constant during epitaxial growth promotes non-radiative charge carrier recombination and prohibits implementing more Ga-rich GaInP top absorbers to approach this optimum. Note that the calculation in Fig. 8(a) bases on assuming optically thick absorbers. Of course, top absorber thinning may enable a similar redistribution of sub-cell current and 19% efficiency prospects, but with the sacrifice of surplus potential neither available for using abundant catalysts nor for generating higher value reaction products. In contrast, a reduction of the bottom absorber band gap (orange arrow) represents the most effective design modification towards 24% STH prospects given sufficient surplus potential compensating the implied loss of voltage.

The development of metamorphic growth techniques (section 3.2.2) eventually enabled graded buffer layers to change III-V lattice constants during epitaxial growth without prohibitive sacrifice of material quality. Both growth cost and material performance goals still limit the design flexibility. In practice, a single graded buffer stack increased the lattice constant to some GaInAs composition before growing the entire tandem structure. Overall lowered bandgaps harvest more of the solar flux than the classical GaInP/GaAs tandem design, but bandgap combinations remain linked (to vertical combinations of red and blue lines in Fig. 8b). The principle trade-off described above remains. For instance, the 1.78 eV/1.26 eV combination (section 3.2.2) features off-optimum efficiency prospects of about 20.8% for thick absorbers. Prospects of over 22% are accessible theoretically with a 1.85 eV top junction and practically by top-absorber thinning, with and without the ability to harvest additional potential.

In contrast, full flexibility to combine arbitrary III-V bandgaps according to theoretical prediction represents a major milestone for advancing solar fuel research. Once achieved, both theory could finally serve as valuable guidance for advanced device design and experiments could finally validate theoretical predictions of increasing complexity (section 2). Beyond enabling new STH conversion records and structural advances, the transfer of inverted metamorphic multijunction (IMM) growth techniques from PV context<sup>81</sup> finally enables dedicated

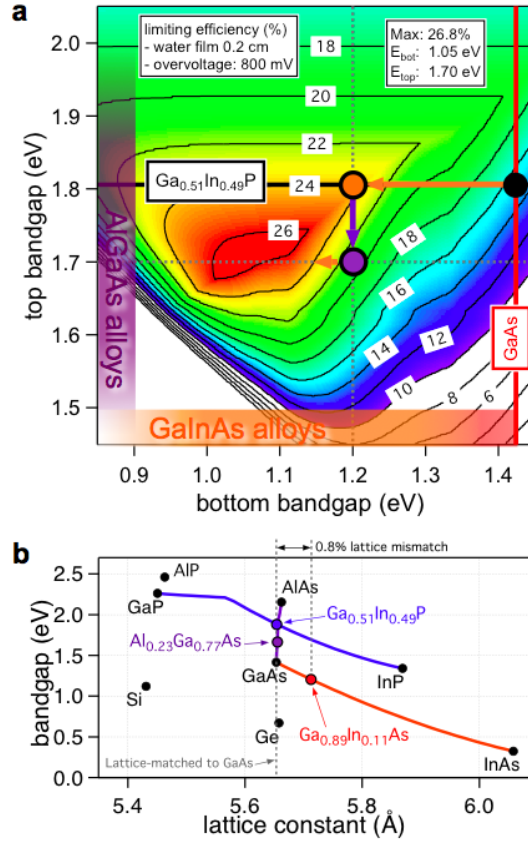


Figure 8: (a) Solar-to-hydrogen isoefficiency contour plot and (b) bandgap vs. lattice constant for various III-V alloys. Reproduced from Ref.<sup>45</sup>.

PEC device design independent of the plain utilization of pre-existing solar cell structures.<sup>45</sup> In contrast, a novel GaInAsP/GaInAs PEC tandem structure transferred back to PV set a new landmark efficiency record of 32.6% for dual-junction solar cells operated without sunlight concentration.<sup>82</sup>

IMM devices are grown inverted with the eventual illuminated side grown first followed by the graded layers and the bottom junction. Substrate removal during post-growth processing allows for the device to be re-oriented. This strategy has a distinct advantage over a more traditional upright growth. Because the top junction generates a higher voltage than the bottom junction – and therefore, a larger fraction of the total power – good material quality in the top junction is essential to high overall efficiency. The inverted-growth architecture allows the lattice-matched top junction to be grown with very few defects and excellent material quality. Deleterious effects, if any, from the dislocations that result from the lattice mismatch are largely confined to the lower-power-producing bottom junction.

After growth, a 1- $\mu\text{m}$ -thick gold film is deposited on the back surface of the device to act as both a rear ohmic/electrical contact and a photon reflector. In the latter capacity, the gold film allows the bottom cell to be thinned by about a factor of two while maintaining the same effective absorption volume, thus enabling a cost reduction. If the junction quality is high enough, the reflector can also enhance the photon recycling to increase the voltage.<sup>83</sup> The device is then bonded to a flat, rigid “handle” to provide mechanical support (such as

a silicon wafer<sup>45</sup>) with epoxy and the GaAs substrate is removed, leaving the wide-bandgap top junction as the uppermost layer. For research purposes, the substrate is usually removed by selective chemical etching, but emerging techniques such as spalling<sup>84</sup> or epitaxial lift-off<sup>85</sup> intend to enable reuse of the GaAs substrate, which is  $\sim 100\times$  thicker than the IMM device and one of the largest cost driver for III-V epitaxy.<sup>86</sup>

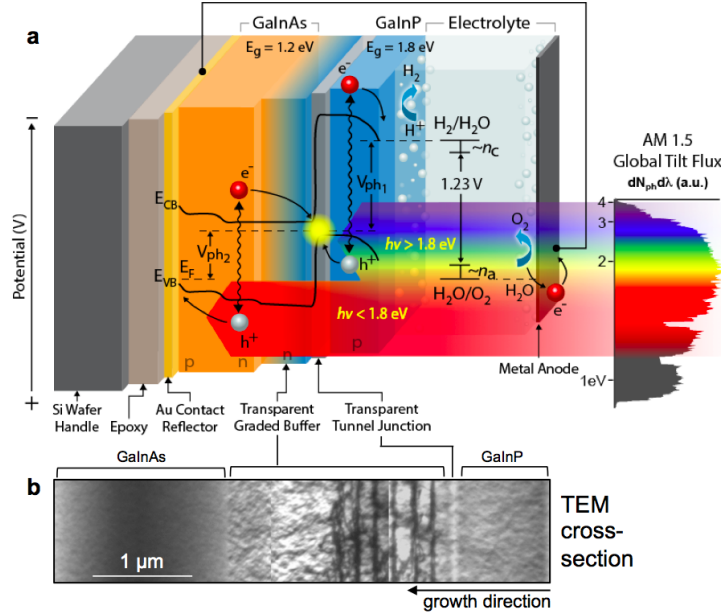


Figure 9: (a) Schematic of IMM configured for water splitting, (b) TEM cross-section of IMM device highlighting the transparent, compositionally graded buffer (CGB) layer and the transparent tunnel junction. Reproduced from Ref.<sup>45</sup>.

Figure 9 shows a schematic of the groundbreaking 1.8/1.2 eV GaInP/GaInAs IMM PEC device.<sup>45</sup> The incident solar flux is split between the top GaInP and bottom GaInAs junctions that are series connected via a transparent tunnel junction. At the PtRu-modified semiconductor/electrolyte interface, conduction-band electrons reduce protons to evolve hydrogen gas while water is oxidized at a metal anode, producing oxygen and protons. The transparent, AlGaInP-based compositionally graded buffer layer stack (CGB) is indicated in the Fig. 9(b) transmission electron microscopy (TEM) cross-section. Dislocations are necessary to change the lattice constant and access lattice-mismatched material, and are observed throughout the transparent CGB. However, the CGB largely confines the dislocations and prevents them from penetrating into the lower junction, thus maintaining device performance.

Figure 10 summarizes recent progress towards optimum STH conversion with IMM PEC devices,<sup>45</sup> indicating relevant device structures (Fig. 10a), associated IPCE (Fig. 10b), and valid on-sun<sup>80</sup> current density-voltage (J-V) measurements (Fig. 10c). Six monolithic, III-V tandem water-splitting devices (characterized coupled to a RuO<sub>x</sub> anode) represent several structural advances achieved:

- LM-upright: Classical GaInP/GaAs lattice-matched, upright PEC/PV tandem.<sup>52,80</sup>
- LM-inverted: Inverted implementation of an analogue GaInP/GaAs device confirming the inverted growth and processing and demonstrating the advantages of the Au back

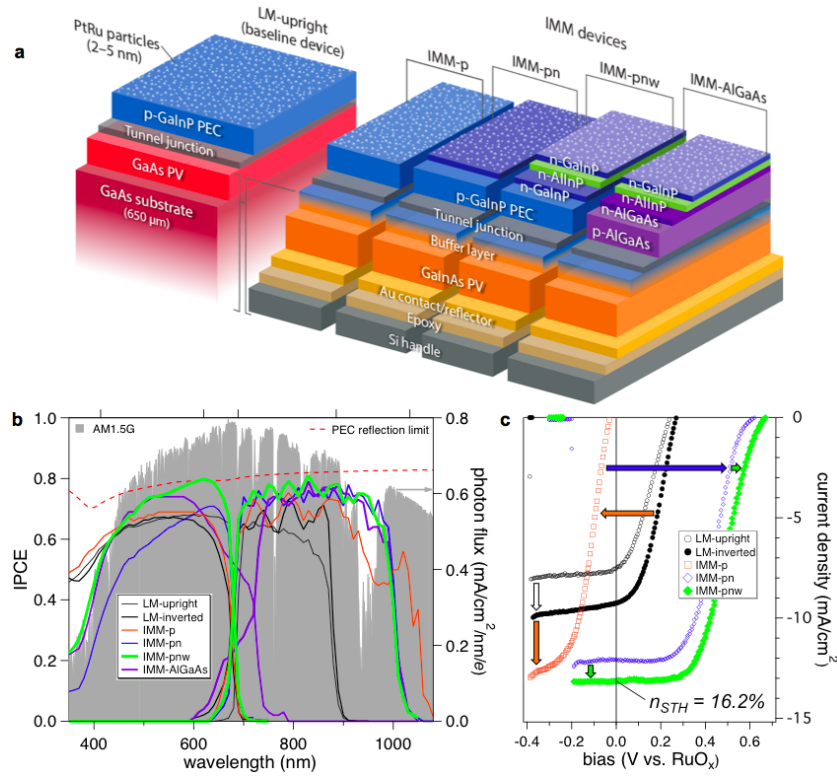


Figure 10: (a) Schematic of tandem structure advances, (b) IPCE, and (c) on-sun J-V characterization. Reproduced from Ref.<sup>45</sup>.

reflector.

- IMM-p: IMM GaInP/GaInAs device with 1.2 eV ( $\text{Ga}_{0.89}\text{In}_{0.11}\text{As}$ ) replacing the GaAs bottom junction.
- IMM-pn: A p-n architecture implemented by a thin (25 nm or less), electrolyte-adjacent n-GaInP layer optimizes photovoltage.
- IMM-pnw: Addition of 20 nm-thick n-AlInP surface passivation and 10 nm n-GaInP capping layers.
- IMM-AlGaAs: Proof-of-principle IMM AlGaAs/GaInAs device (replacing the GaInP with 1.7 eV  $\text{Al}_{0.23}\text{Ga}_{0.77}\text{As}$ ) as a first step towards yet higher STH conversion (see Fig. 8).

The LM-upright structure<sup>80</sup> basically reproduces the classical design<sup>52</sup> and serves as reference. IPCE characterization (Fig. 10b) confirms decent external quantum efficiency (grey line) on the order of 60% throughout the relevant parts of the solar spectrum for both GaInP top ( $\geq 1.8$  eV) and GaAs bottom ( $\geq 1.4$  eV) junctions. Reflection off the device (and PEC cell) surface already diminishes the solar flux before reaching the absorber layers by about 20% (thin dashed red line), but some room for improvement remains. Integration of the quantum efficiency over the solar irradiance spectrum (light grey area) shows a significant current mismatch between top and bottom junction (11.9 vs. 7.8  $\text{mAcm}^{-2}$ ), in line with unbiased on-sun water-splitting operation at 7.6  $\text{mAcm}^{-2}$  (Fig. 10c) or about 9.3% STH efficiency. The LM-inverted design

consists of identical materials, but highlights a major advantage of the inversion procedure. Substrate removal enables Au back contact deposition directly on the epitaxial GaAs absorber material, where it also serves as an efficient back reflector effectively preventing photon losses. IPCE (Fig. 10b, black line) shows significant improvements of the long-wavelength response and interference oscillations. In combination with some current re-distribution by slightly thinning the top absorber, an on-sun performance of  $9.3 \text{ mAcm}^{-2}$  (Fig. 10c, black line) or 11.4% STH could be achieved.

The IMM-p device represents a first step towards utilizing the design flexibility enabled by inverted metamorphic III-V epitaxy. The novel bandgap pairing between GaInP (1.8 eV) and GaInAs (1.2 eV) successfully lifts the current limitation by the bottom absorber. Its spectral response extends significantly towards longer wavelengths (Fig. 10b, orange line) with an integrated current density of  $14.8 \text{ mAcm}^{-2}$  for the bottom junction. The light-limited photocurrent of the tandem increases to above  $12 \text{ mAcm}^{-2}$  (Fig. 10c, orange). However, the photocurrent-for-photovoltage tradeoff (orange arrows) inherent to the lowering of the bottom bandgap resulted in insufficient photovoltage to drive the water splitting reaction (0% STH). This highlights the necessity of understanding the critical design criteria for maximum water-splitting efficiency: Photocurrent density (and thus efficiency) is maximized with lower-bandgap energy pairings with the critical constraint of maintaining sufficient photovoltage for water splitting.

Apparently, all previously discussed devices suffer from excessive overvoltage losses. Among various mechanisms the band-edge energetics of the PEC junction contributes a significant share. The conduction band of GaInP aligns about 0.6 V above the hydrogen evolution reaction potential.<sup>87</sup> In principle, hydrogen evolution at high rates requires only about 50 mV overpotential.<sup>88</sup> Due to the corresponding offset in the valence band and bulk Fermi levels, the holes reaching the electrolyte via the anode come with reduced (and in the IMM-p case insufficient) oxidative potential for the oxygen-evolution reaction.

The implementation of a p-n homojunction serves to utilize the excess overpotential at the GaInP electrolyte interface for an effectively enhanced and tunable photovoltage. Actually, the IMM-pn device produces a near-optimized photovoltage that is 0.55 V higher (Fig. 10c, blue arrow) compared to IMM-p. Earlier studies indicate that such a "buried junction" device forms a simple ohmic contact at the electrolyte, but do not consider band bending of the n-type layer.<sup>89</sup> The n-GaInP in the IMM-pn produces upward band bending toward the electrolyte that lowers the conduction band systematically with thickness and doping density, allowing the excess overpotential to be reduced. The IMM-pn device shows unbiased water splitting at  $11.5 \text{ mAcm}^{-2}$  (Fig. 10, blue) or 14.1% STH. The IPCE analysis (Fig. 10b, blue line) uncover insufficient quantum conversion efficiency of the current limiting GaInP top junction, in particular towards shorter wavelengths. Presumably, the upward band bending in the n-GaInP layer hinders the transport of holes generated near the surface, which are subject to increased non-radiative recombination then.

Integration of a thin n-type AlInP window layer on top of the IMM-pn device results in much better surface passivation as demonstrated by much improved top junction IPCE of the IMM-pnw device (Fig. 10b, green line). AlInP has a relatively wide, indirect bandgap and is highly transparent, with its conduction band aligned to that of GaInP to ensure facile electron transport to the electrolyte. The deep valence band provides passivation by blocking minority-carrier holes from surface recombination sites while also counteracting the upward band bending of n-GaInP that occurs when in contact with electrolyte. Because aluminum-containing semiconductors such as n-AlInP are unstable in contact with aqueous electrolyte, the device also includes another thin n-GaInP capping layer for surface protection. Despite

some parasitic absorption occurring in the capping layer mostly effecting shorter wavelength, the design enables a significant net improvement of the unbiased water-splitting performance to  $13.2 \text{ mAcm}^{-2}$  (Fig. 10c, green line) or 16.2% STH efficiency. The on-sun characterization of the IMM-pnw device clearly demonstrates its excellent photovoltage, letting it achieve its light-limited photocurrent more than 200 mV earlier than necessary.

The design flexibility of the IMM PEC device concept enables a dedicated trade-off of such surplus photovoltage for higher photocurrent by designing a device with lowered top and bottom junction bandgaps. The IMM-AlGaAs structure represents a proof-of-principle for a first step in that direction. As outline in Fig. 8(a), AlGaAs compositions replacing the top junction, enable a bandgap reduction targeting 1.7 eV (purple arrow). In a second step, further reduction of the GaInAs bottom absorber bandgap by further In incorporation (orange arrow) may restore current-matching and effectively exploit additional solar flux at longer wavelengths. Initially, top absorber thinning serves for current matching instead (Fig. 10b, purple lines). Due to stability issues, the top junction material might need to be replaced by GaInAsP<sup>90</sup> with a composition enabling the target bandgap of 1.7 eV.

## 4 Efficiency measurement and characterization strategies

Tandem (or multi-junction) absorber structures constitute a requisite for high efficiency solar energy conversion. Beyond the effective capture of the energy distributed over the sunlight spectrum in general, the chemical potentials involved in solar fuel generation dictates device operation at (rather high) voltages discouraging the use of simple single-junction absorbers due to the significantly lower currents that result. In the most prominent case of unbiased solar water splitting operation, both theory (section 2) and experimental implementation (section 3) clearly demonstrate the need for specifically designed dual-junction structures for achieving optimum performance. The increased structural complexity (multiple absorbers as well as their electronic interconnect) triggers a chain of challenges beginning with the dedicated design of optimum device structures and the ability for their experimental implementation – quickly leading to the question of adequate and accurate characterization. Most prominently, solar-to-hydrogen (STH) conversion efficiency serves as the primary figure of merit for both scientific progress and potential commercialization options. Therefore, our discussion of regularly overlooked measurement issues and advisable techniques centres on the ability of determining reliable, realistic, and valid STH efficiencies. Of course, other quantitative characterization methods equally benefit from enhanced measurement accuracy. Without, even qualitative analyses based on sample-to-sample comparison can produce misleading conclusions.

### 4.1 Standard solar irradiance vs. laboratory light sources

We have already discussed the critical impact of flux distribution within the illumination spectrum on the efficiency prospects and design guidelines for solar fuel devices above (section 2) where the parasitic sunlight absorption in aqueous electrolyte and catalyst shaped the effectively available irradiance on the absorber level. In practice, laboratory characterization requires artificial illumination, but the available light sources strongly deviate from the solar spectrum, even in the case of so-called solar simulators. Figure 11 displays optical emission spectra of typical illumination sources used for PEC characterization (acquired with a Stellar-Net spectrometer) compared to solar irradiance (global, air mass 1.5, ASTM G173-3).<sup>80</sup> Note that in analogy to a classical pyranometer (or thermopile) calibration, intensities are set to equivalent power within the relevant wavelength regime (280–1800 nm), which comprises more than 95% of terrestrial solar power (1 kW/m<sup>2</sup>). Global intensity adjustment remains the only calibration parameter for a given light source, while the mismatch of flux distribution strongly depends on the relevant spectral region, i.e. the bandgap and absorption characteristics of the specimen. Both multi-exciton generation and hot carrier extraction remain negligible in classical absorber materials, where each absorbed photon eventually generates a pair of thermalized charge carriers. Hence, the use of photon flux units (rather than power units) in Figure 11 provides for direct proportionality to current generation potential at the given wavelength. Spectral integration then yields the theoretical current limit (for unity light absorption and charge-carrier extraction) associated with each absorber bandgap — an important measure for sub-cell current matching in tandem device design and for overall advances in STH conversion efficiency.

Despite being calibrated to provide solar-equivalent power, all laboratory white-light sources (e.g. those shown in Figure 11) deviate from the standard solar flux distribution and introduce significant error in absorber current limits for most bandgaps, though recent developments of multi-LED solar simulators promise advances here. For tandem absorbers, this effect is

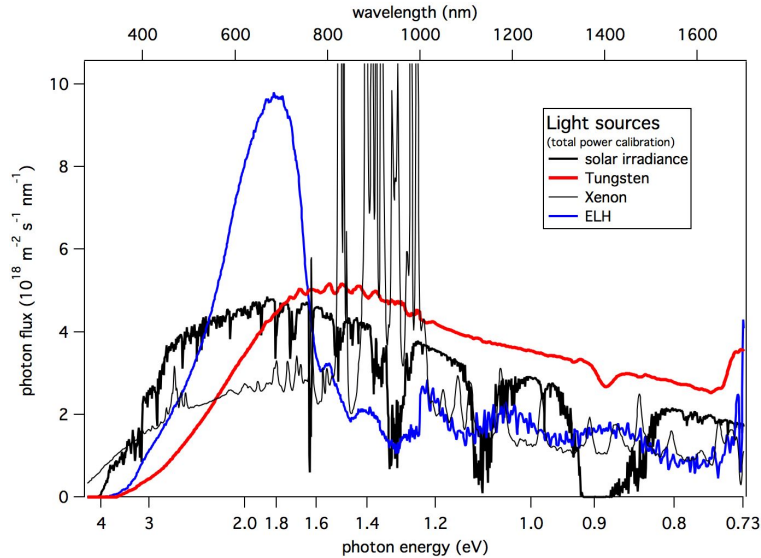


Figure 11: Spectral distribution of flux for AM1.5 global irradiance compared to typical PEC laboratory white-light sources (adjusted to provide solar equivalent illumination power). Reproduced from Ref.<sup>80</sup> with permission from the RSC. ELH: Tungsten halogen lamp with dichroic reflector.

smallest for bandgap combinations that are ideally adapted to the (real) solar spectrum and show perfect current matching. With the number of junctions and the degree of non-ideality, the magnitude of this error will typically increase.

Laboratory light-source calibration approaches often rely on calibrated reference PV devices instead of a spectral power measurement. Adjusting the light-source intensity to achieve the calibration current with the reference solar cell placed at the measurement position removes systematic deviation of the current limit — when, and only when, testing absorbers with equal bandgap. Figure 12 exemplifies the approach using a GaInP reference solar cell. At its bandgap energy of 1.81 eV, all light sources produce a solar-equivalent current-density limit of 19.4 mA/cm<sup>2</sup>, but the spectral distribution of flux still strongly depends on the source type. The calibrated emission flux of the tungsten lamp actually only equals AM1.5 global solar irradiance around 2.2 eV; the source systematically lacks emission in the ultraviolet (UV) range, but is compensated by an adequate excess of intensity in the visible range. In contrast, the xenon source produces a significant surplus in UV emission as well as excessive characteristic emission lines in the near infrared (NIR) region, particularly in the range of 800-1000 nm (1.2-1.6 eV).

In general, the light-source calibration implies substitution of photon count between different emission wavelengths. Results are only valid in the case where photon absorption and charge-carrier extraction probabilities are independent of the excitation energy. Both the reference cell and the tested material must comply with this idealized absorbed condition (IAC), which is essentially equivalent with an experimental finding of constant IPCE above the respective bandgaps. Explicit IAC violations include advanced absorber concepts (multi-exciton generation, upconversion), molecular materials (dye sensitization, organic materials), and light management (photonic coupling, absorber thinning). In general, non-abrupt absorption edges affect virtually any semiconductor to some extent, but in particular Si and other indirect tran-

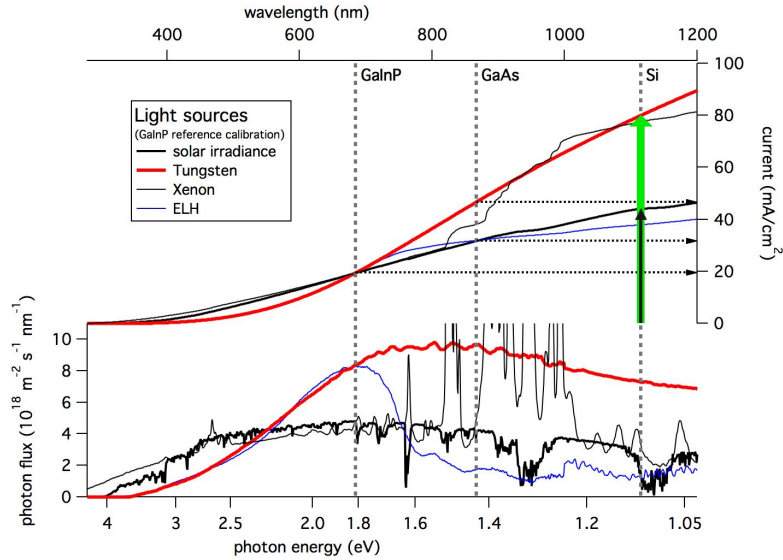


Figure 12: Current limitation vs. absorber bandgap for AM1.5 global illumination as well as for various laboratory white-light sources (top) based on reference-cell calibration exemplified for an externally calibrated GaInP reference solar cell. Reproduced from Ref.<sup>80</sup> with permission from the RSC.

sition materials. In contrast, high-efficiency water-splitting devices generally require nearly ideal absorber materials, and their particular implementation with advanced III-V semiconductors goes along with good IAC compliance. Nevertheless, the requisite for tandem absorber designs still impedes the ability of straight-forward STH efficiency characterization with typical laboratory light sources due to their solar-inequivalent flux distribution.

## 4.2 Tandem device characterization: a case study on common practice vs. result validation

The impacts of solar-inequivalent laboratory light sources include both absolute misjudgment (often tremendous overestimation, even for single-junction absorbers<sup>23</sup>) of critical performance parameters including STH efficiency and precarious misinterpretation of relative results. For exemplification of these trends in the case of a tandem absorber, we discuss measurements of the classical GaInP/GaAs tandem structure design. In detail, we report on an improved upright epitaxial III-V tandem PEC structure grown by metalorganic vapour-phase epitaxy<sup>75</sup> (Fig. 13) that closely matches the three main features of the classical GaInP/GaAs design<sup>52</sup>: (i) An optically thick, epitaxial,  $4\ \mu\text{m}$  p-type GaInP top absorber ( $\text{Ga}_{0.51}\text{In}_{0.49}\text{P}$  composition, 1.81 eV bandgap energy) forming the hydrogen-evolving PEC junction with the electrolyte at its surface; (ii) a buried GaAs bottom junction on a single-crystalline GaAs(100) substrate as joint growth template providing a PV bias to drive the water-splitting reaction without external voltage supply; and (iii) a tunnel junction for electrical series-connection of both sub-devices in a tandem configuration. Structural advances of the current design include aluminium incorporation in the tunnel junction, window layer, and back-surface field for better performance and lower parasitic absorption, as well as a heterojunction GaAs bottom cell and a sputtered PtRu co-catalyst. Figure 13(b) demonstrates traditional laboratory-based STH

conversion-efficiency characterization. In a two-electrode configuration measured vs. an  $\text{IrO}_2$  counter electrode, we observe a direct water-splitting operation driven by a tungsten white-light source (with 3" water filter) set at a 1-sun intensity (at pos. A of Fig. 18) employing a calibrated GaInP reference solar cell. At short-circuit condition (referring to the absence of an external bias potential), we observe a current density of  $17.7 \text{ mA/cm}^2$  (on an  $0.085 \text{ cm}^2$  sample), indicating an "STH" (inflated, as discussed below) conversion efficiency of 21.8%.

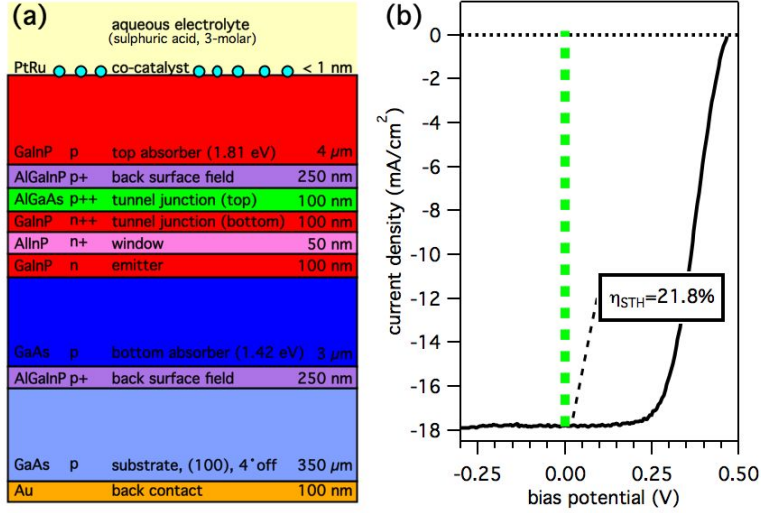


Figure 13: (a) Improved upright epitaxial GaInP/GaAs tandem PEC device structure and (b) current density vs. voltage characteristic of a  $0.085 \text{ cm}^2$  sample under tungsten white-light illumination adjusted with GaInP reference. Here, " $\eta_{\text{STH}}$ " is subject to errors, as discussed in the text. Reproduced from Ref.<sup>80</sup> with permission from the RSC.

In comparison, dotted horizontal arrows in Fig. 12 mark the expected GaInP ( $19.4 \text{ mA/cm}^2$ ) and GaAs ( $31.7 \text{ mA/cm}^2$ ) light levels for AM1.5 global illumination. The optically thick top absorber (Fig. 12a) provides sufficient absorption length to filter all sunlight above its bandgap energy. In principle, the residual bottom-cell illumination light level of  $12.3 \text{ mA/cm}^2$  should then constrain the series-connected device performance as the current-limiting junction. Although the historic result<sup>52</sup> still appears compatible (82%) with that fundamental limitation, our current data indicated a clear violation (144%).

Critical evaluation of the illumination light-source used (Fig. 12) quickly reveals a significant systematic error in our experimental configuration, causing a drastic overestimation of STH conversion efficiency: The spectral emission shape of the tungsten source causes a vast relative over-illumination of the GaAs bottom junction, associated with an effective bottom sub-cell light level of  $27.3 \text{ mA/cm}^2$  (instead of  $12.3 \text{ mA/cm}^2$  for AM1.5 global; both values subsequent to GaInP filter) when using a GaInP reference cell for intensity adjustment at 1-sun level. In effect, the much lower light level of the GaInP top absorber ( $19.4 \text{ mA/cm}^2$ ) then imposes the current limitation of the tandem device for the laboratory measurement — in contrast to the situation in actual sunlight. In principle, the light-level ratio of an ELH source as used in Ref.<sup>52</sup> appears much better (Fig. 12), but the spectral distribution strongly deviates from solar irradiance, and we cannot exclude significant calibration error affecting the historic

measurements. Note that our tandem result (Fig. 13) still requires 91% quantum conversion of the incident light in the GaInP top junction.

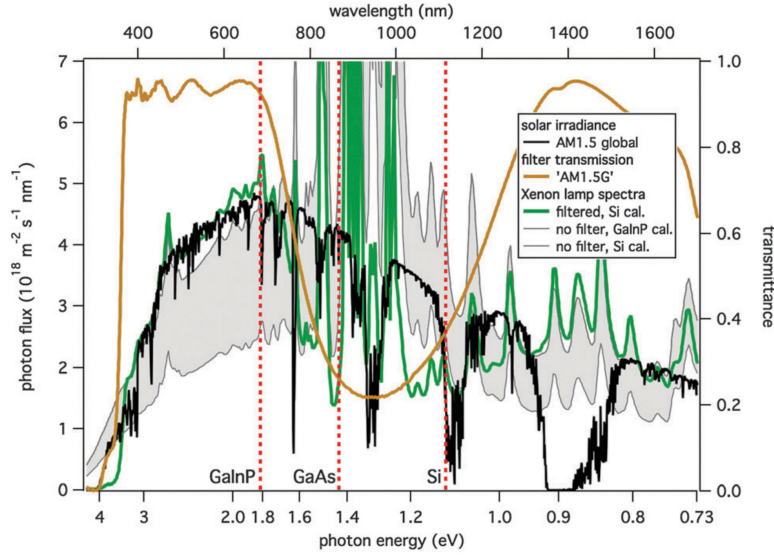


Figure 14: Transmission spectrum of an Oriel AM 1.5G optical filter (yellow) as well as filtered (green) and unfiltered (grey) xenon arc lamp spectra (various calibrations) in comparison to AM 1.5 global solar irradiance. Reproduced from Ref.<sup>80</sup> with permission from the RSC.

Even for simpler single-junction configurations, PEC characterization is particularly susceptible to spectral mismatch issues: The high voltage requirement for unassisted water-splitting particularly focuses high-bandgap materials and, accordingly, the high photon-energy onset of the solar spectrum — despite the minor contribution of the UV region to the total solar current-generation potential. The fundamental deviation of white-light-source emission shapes (Figs. 11 and 12) accentuates the mismatch, with only little chance for suppression through intensity calibration. For instance, xenon-emission-based illumination systems fundamentally over-supply the UV range, whereas tungsten sources fall short in that region. Popular solar simulators consist of xenon arc lamps with specific optical filters for spectral modification. Figure 14 displays the transmission spectrum of the widespread Oriel AM1.5G filter (yellow), featuring a steep UV cut-off around 3.6 eV, a broad attenuation feature in the near IR (between 1.0 and 1.6 eV), and more or less constant transmission (close to unity) anywhere else. Its application to the native xenon lamp spectrum (grey, various calibrations) creates a somewhat closer match (green) to the AM1.5 global solar irradiance standard (black): Still, flux distributions only agree well in the visible range, but both UV cut-off and near IR attenuation induce a certain balance of photon surpluses and deficits within either region. Among a pyranometer, Si and GaInP references, intensity calibration deviates only marginally (by a few %). Also, the light levels for individual absorbers (e.g. 102.6% for GaInP or 98.6% for GaAs, both based on Si reference) appear fairly reasonable. In contrast, the light source configuration fixes incorrect light level ratios for tandem devices, such as 1:0.895 for our exemplary GaInP/GaAs structure. Intensity calibration may only decide whether to over-/undersupply the top/bottom absorber by this factor, but the overall performance of tandem absorbers critically depends on current matching between the sub-devices. Hence, both absolute STH efficiency figures and

qualitative insights for advanced tandem device development may be flawed significantly.

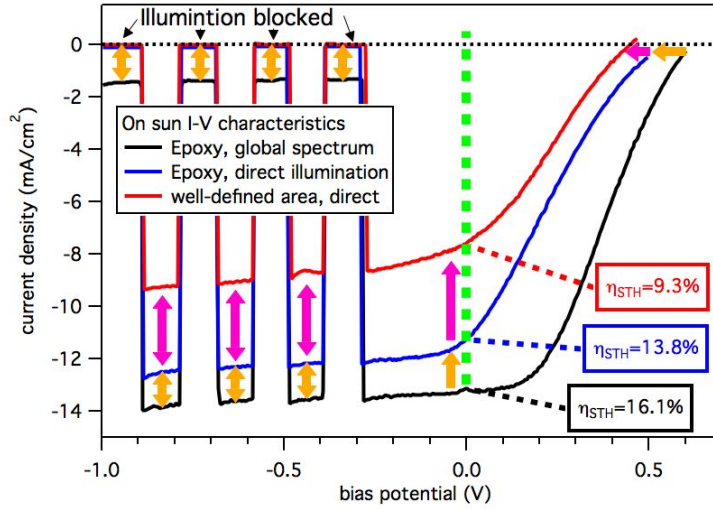


Figure 15: Water-splitting characteristics measured with actual sunlight (outdoors) for standard epoxy PEC tandem cathodes vs.  $\text{IrO}_2$  anodes with normalized global (black) and direct (blue) illumination in comparison to proper area definition (red); current density at zero bias (green dashed line) is considered as indication of STH conversion efficiency  $\eta_{\text{STH}}$ , whereas only the red curve is a real  $\eta_{\text{STH}}$  value. Reproduced from Ref.<sup>80</sup> with permission from the RSC.

### 4.3 Utilization of natural sunlight and secondary illumination errors

For minimizing the spectral-mismatch error, outdoor PEC characterization was conducted under sunlight illumination. Of course, both the intensity and spectral composition of the terrestrial sunlight spectrum depend strongly on factors such as season, angle of incidence, air pollution, and altitude. All results shown in Fig. 15 were measured in Golden, CO, USA, in the direct vicinity of the NREL Solar Radiation Research Laboratory, where precise data on actual solar irradiance are continuously recorded and published.<sup>91</sup> All the data were normalized following the established PV convention of assuming  $1 \text{ kW/m}^2$  intensity as a 1-sun illumination level regardless of the applied spectrum.<sup>92</sup> The spectral mismatch between the applied sunlight and the solar irradiance standards was mitigated by appropriate timing (to ensure nearly AM1.5 global conditions). It still remains a potential source of error (less than 5%<sup>23</sup>), but of negligible magnitude at the present accuracy level of PEC STH efficiency determination.

In a first attempt for the structure shown in Fig. 13, we found unbiased water-splitting operation driven only by sunlight to occur beyond  $13 \text{ mA/cm}^2$  current density for a calculated 16% STH conversion (Fig. 15, black line). The values fell below the initial laboratory characterization result (Fig. 13b), but still greatly exceeded experimental limits derived from quantum conversion reference characterization obtained with incident photo to current efficiency measurements (IPCE, see below). Apparently, additional factors contributing to STH overestimation beyond an inadequate choice of illumination source. Significant current levels while blocking the direct light path (Fig. 15, black line) confirmed indirect device illumination that is part of the global solar spectrum, but the effect could be artificially enhanced by the

glassware instrumentation surrounding the PEC sample. Indirect light paths were excluded by using a dark compartment around the PEC cell, where the device is exclusively illuminated through a collimating tube<sup>93</sup> designed to restrict the incident sunlight to the direct and circumsolar ( $5^\circ$  field of view) portion. In that configuration, the current density above  $11 \text{ mA/cm}^2$  (Fig. 15, blue line) indicates almost 14% STH conversion. Note that normalization to the  $1 \text{ kW/m}^2$  1-sun convention<sup>92</sup> enables the direct comparison between the current densities shown in Fig. 15, despite the change from global to direct irradiance.

Inappropriate active-device-area definition and confinement remained the last area of possible experimental deficiency to explain the residual overestimation of PEC performance. Epoxy encased electrode construction is common throughout the scientific community for simplicity, flexibility, and corrosion resistance. Downsides can include: sample-to-sample variation of device area, unexpected under-etching or interaction with the electrolyte, and optical impact of light reflection and/or transmission. In an effort to exclude epoxy from impacting our results, an alternative, compression-type PEC cell design was used, where an inert O-ring precisely defines the active area (of  $0.185 \text{ cm}^2$ ); the rest of the sample area was shielded with Al foil to avoid unintentional illumination. The result (Fig. 15, red line) might be perceived as a huge drop in PEC performance to about  $7.6 \text{ mA/cm}^2$  in current density or 9.3% in STH conversion. Actually, the values show remarkable consistency with experimental current limitations estimated by IPCE (Fig. 16). Pragmatically, only that final number truly represents the STH energy-conversion efficiency (unity Faradaic efficiency provided, i.e., absence of sacrificial reactions, to be confirmed by consistent gas chromatographic product analysis), whereas the device performance was significantly overrated in all earlier measurements due to uncontrolled systematic errors.

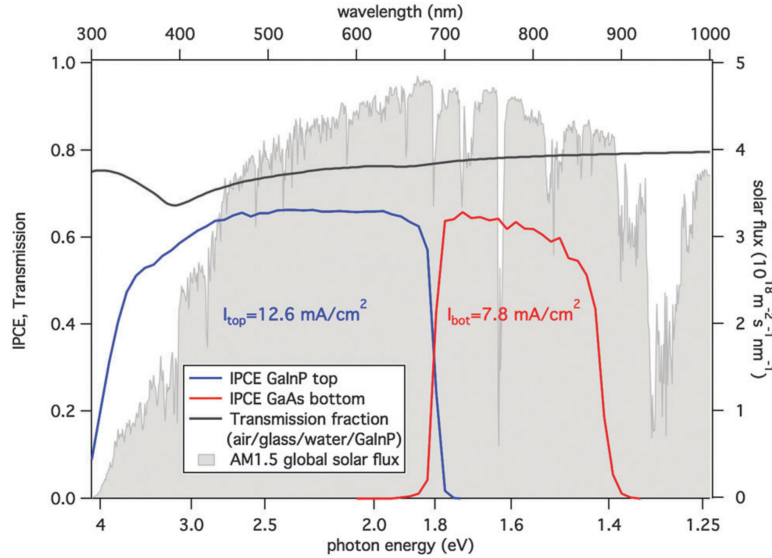


Figure 16: Independent IPCE characterization of GaInP top (blue) and GaAs bottom (red) absorbers of our PEC tandem device acquired with appropriate bias illumination; modelled transmission through air/glass/electrolyte/semiconductor interface system (dark grey); and AM1.5 global solar flux (light grey area). Reproduced from Ref.<sup>80</sup> with permission from the RSC.

In total, typical—but inappropriate—PEC testing techniques led to a major inflation of the

estimated STH performance—in this case, to more than double (17.7 vs. 7.6 mA/cm<sup>2</sup>) the correct value was obtained with advanced techniques inspired by multijunction PV characterization. Beyond primary illumination errors (regarding the light source spectral mismatch and intensity calibration), secondary deficiencies may also contribute significantly to overrated performance observations. In order to understand the insufficiencies related to epoxy-encased electrodes, the spectral transmission properties were measured of our exemplary Loctite HySol 9462 epoxy (Fig. 17) that we used for laboratory-scale PEC electrode assembly. The inset in Fig. 17 illustrates the assembly concept: Rectangular semiconductor absorbers usually receive an external electrical back-contact with Ag paint and Cu wire before the entire device, except the central area of the front surface, is coated by a chemically inert epoxy to prevent contact with the reactive electrolyte during operation. Epoxy layer thicknesses in the order of 1 mm ensure proper illumination-area definition because the thinnest layers (0.1 mm) appear optically semi-transparent. The optical transmission spectra of defined epoxy films confined between two glass slides (Fig. 17) demonstrate significant penetration even through thicker layers. In a simple absorbance model (Fig. 17, dashed lines), transmission of the air/glass/epoxy/glass/air layer stacks should only depend on reflection of interfaces (constant) and absorption in the epoxy (exponential decay). Calculations do not reproduce the data, but indicate sub-exponential behaviour consistent with significant translucence of the epoxy, probably based on scattering of incident light.

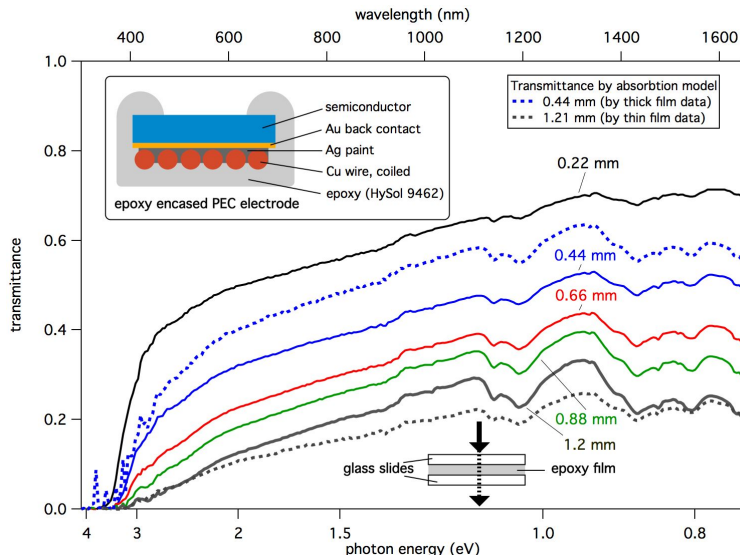


Figure 17: Spectral transmission through Loctite HySol 9462 epoxy films confined between glass slides, as well as schematic diagram (inset) of the epoxy-encased PEC electrode manufacturing concept. Reproduced from Ref.<sup>80</sup> with permission from the RSC.

The consequence is an imprecise area definition for PEC devices, where the epoxy only defines the chemically active surface area, but also allows for partial illumination of the covered area (Fig. 17, inset). The contribution to device performance remains largely unpredictable because epoxy thickness and the fraction of covered area vary, additionally, the lateral collection of charge carriers plays a significant role. Scanning light-spot analysis could provide the means to quantify this error,<sup>94</sup> but analysis must take into account that the reaction area is larger than the illuminated area, which benefits catalysis. Based on higher light transmission and

better charge-carrier transport, the limiting GaAs bottom junction might benefit more than proportionally in epoxy-encased electrode configurations. Both effects supposedly contribute most for small, research-scale samples. An active area of about  $0.085\text{ cm}^2$  was used for epoxy electrodes represented in this study. A brief statistical survey over the range of  $0.02\text{--}0.06\text{ cm}^2$  samples (20 pieces) from the same growth run did not show an evident correlation between active area and observed light-limited photocurrent. Other epoxy types provide more desirable light-transmission properties, but complete opacity to the full solar-irradiance spectrum remains to be confirmed. The error for the area definition can be greatly reduced by the use of black high-viscosity epoxy (e.g. the Electrolube ER 2162 or 1455 used in<sup>43</sup>), which enables steep edges to minimise imprecise areas due to edge creep. Larger-area samples, where only a small fraction of the absorber surface is covered by the epoxy, further reduces the error of area and a partially transparent epoxy. The latter approach also reduces the dark current, which benefits photovoltage and consequently efficiency. For more discussion on various epoxy-related issues, see chapter "Prototyping Development" in the present book.

In general, the light path between the chosen illumination source and the defined illumination error constitutes another source of potential measurement error and possible efficiency overrating. The contribution of unintended indirect light paths inducing an illumination (and according photocurrent) surplus was described above. Our solution (dark compartment and collimating tube) implies the switch to direct irradiance in good consistency with the most likely application scenario of highest efficiency water splitting devices. Operation under mild to intermediate sunlight concentration may help to compensate rather high materials and production costs. The outdoor characterization approach with natural sunlight circumvents not only the spectral mismatch of laboratory light sources, but also issues related to the divergent nature. In combination with the specific PEC operation scenario (within an electrochemical cell, made from glass or with glass windows, filled with aqueous electrolyte) potential error mechanisms regarding the light source intensity calibration and unintentional illumination concentration require consideration.

In principle, light level adjustment based on an appropriate PV reference device promises highest accuracy when done at place, but in absence of the PEC cell (position A in Fig. 18). In contrast, intensity calibration in dry (air-filled) or wet (electrolyte-filled) *outer* PEC cells (position B in Fig. 18) is subject to additional inaccuracies and possible systematic performance inflation. Neglect of the reflective loss at the additional air-glass interfaces (approximately 4% per pass) during light source intensity adjustment (based on achieving the calibration current of the PV reference cell) will systematically produce a higher (not solar-equivalent) flux level. The error can, however, be reduced by employing filters in combination with the reference cell, as discussed in ref.<sup>95</sup>. For tandem cells, this requires a number of calibrations equal to the number of subcells, each with a suitable combination of filters in front of the reference cell to mimic the transmission of the overlying solar cells as well as a filter for the spectral range between the absorption onset of the reference cell and the bottom solar cell. This multi-step calibration requires a tuning of the illumination source irradiance in the spectral regions of the subcells independently. While this is relatively straightforward for multi-source (e.g. LED-based) solar simulators, it requires the introduction of additional filters for single-lamp sources, where only the overall intensity can be adjusted.

Potential unintentional performance record inflation might be highest when filling the PEC cell after calibration, as the lowered refractive index offset will effectively reduce the reflective loss then. Neglect of the parasitic light absorption in the electrolyte (see section 2) may affect calibrations done in presence of the electrolyte. An artificially overrated light level

would compensate the lost photon flux after a simple adjustment to the calibration current. Common Si-based PV reference devices appear most susceptible, as light absorption in water is most relevant for longer wavelengths. Despite an appropriate intensity calibration, the divergent nature of artificial light sources in combination with a typical cell might finally introduce a slight unintended illumination concentration. Compared to the calibration ideally done in air, the subsequent installation of a typical PEC set-up introduces with the glass window and the electrolyte materials with much higher refractive index into the light path. In consequence, the whole configuration effectively acts as a weak lens.<sup>95</sup> Even high-end solar simulators typically specify a 4° divergence half angle artificially inflating the light level and observed the photocurrent by about 10% in our example (assuming an active area of 0.16 cm<sup>2</sup>, a window thickness of 0.2 cm and an electrolyte film of 0.2 cm).

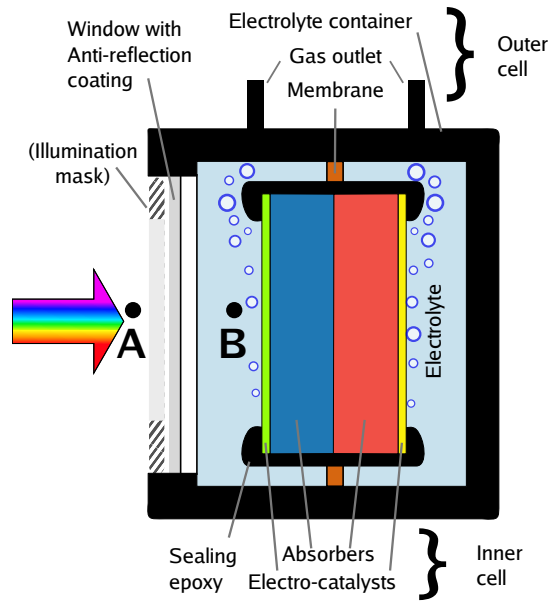


Figure 18: Sketch of a photoelectrochemical cell for efficiency validation with the two points for spectral calibration, A and B. While B reduces errors from global illumination, A is the more realistic point of reference as long as cell components do not act as light concentrating elements. If effects of global illumination and diverging light cannot be excluded, a mask for the definition of the illuminated area has to be used. Adapted from Ref.<sup>15</sup> with permission from the RSC.

#### 4.4 Differential spectral responsivity

Another approach for reliable solar-to-fuel efficiency evaluation is to use multi-source sun simulators employing the spectrometric characterisation technique, the most common approach used in multi-junction photovoltaics.<sup>15,96,97</sup> Here, the integrated spectral responsivity  $s_j$  of a subcell  $j$  under a light source  $i$  with the spectrum  $e_i$  has to deliver the same current as under the absolute spectral irradiance of reference spectrum  $e_{\text{ref}}$  (AM 1.5G), subject to a correction

factor  $A_i$ :

$$\sum_{i=1}^N A_i \int_{\lambda} s_j(\lambda) e_i(\lambda) d\lambda = \int_{\lambda} s_j(\lambda) e_{\text{ref}}(\lambda) d\lambda; j = 1, 2 \dots N \quad (1)$$

The spectral responsivity is measured by a variation of the light source, which in turn is calibrated with a suitable reference cell. The correction factor  $A_i$ , obtained from the linear equation system in eq. 1, gives us then the correction we have to apply to the  $i$ th of the  $N$  subcells.<sup>96,97</sup> Another option would be the extension of the differential spectral responsivity scheme<sup>98</sup> to multi-junction absorbers replacing the white bias light with monochromatic light sources addressing each subcell. This has become feasible with the availability of sun-simulators that employ a large number of independently adjustable LED's. To probe  $s_j(\lambda)$  of a subcell, the bias light of the complementary subcells is set to render the probed cell current-limiting, yet still at near-operational overall current. Then, the differential spectral responsivity (DSR),  $\tilde{s} = \Delta I / \Delta$ , is measured with a monochromatic, modulated probe beam employing a lock-in amplifier. An integration of  $\tilde{s}$  allows us to obtain  $s(\lambda)$ . With this factor, the response of a subcell is again corrected for the mismatch between actual and simulated AM 1.5G spectrum according to eq. 1.

For solar water splitting, conditions near the operating current are necessary because of the non-linearity of catalyst overpotentials and as the optical properties of the device are likely to change because of gas evolution and potential changes in electrolyte composition. The approach has the advantage, that violations of IAC (see above) do not deteriorate the result. Filtering out the signal of the modulated light source at high bias current is, however, a difficult task with the commonly used monochromated lamp sources because of their low spectral irradiance that renders signal recovery almost impossible. Slow charge-transfer kinetics in a water splitting system, which can increase the response time of the system to a change in illumination, aggravate the difficulty. In a recent attempt for photovoltaics, the lamp source has been replaced by a femtosecond laser system with an optical pulse-to-CW converter to increase the spectral irradiance by a factor of about 1000.<sup>99</sup> Even with such a light source, the measurement of the spectral responsivity in a photoelectrochemical environment remains a challenge.

## 4.5 Solar-to-hydrogen conversion reference laboratories

We propose applying the following standards for future PEC performance reporting: (i) traceable disclosure of the illumination-source configuration (lamp, filters, optics, PEC configuration, calibration routine) and/or its measured spectral distribution; (ii) thorough device-area definition (including confinement of the illumination area and avoidance of indirect light paths); (iii) complementary IPCE confirmation of the solar-generation potential or, alternatively, DSR by use of multi-source solar simulators; and (iv) proper consideration of Faradaic efficiency. In the long term, only standardized and validated PEC testing and STH efficiency determination techniques will provide a credible, objective base for scientific progress and technological deployment of solar water-splitting devices for solar fuel generation. The formation of acknowledged reference laboratories analogous to the PV community should be considered.

In benchmarking  $\eta$  STH (or STF for products beyond hydrogen), the protocols should identify and mitigate critical influence factors that introduce measurement errors. Our benchmarking protocol includes: 1) On-sun (i.e. using natural sunlight), direct-only (diffuse excluded)

solar illumination as necessary for accurate and precisely defined illumination, that also mitigates optical concentration effects inherent to diverging-source solar simulators, 2) Incident photon-to-current efficiency (IPCE) or differential spectral responsivity (DSR) measurements for spectral correction, translation of performance measurements to reference conditions such as AM1.5G, and  $\eta$  STH validation including active-area definition, and 3) Confirmation of Faradaic efficiency.

## 5 Summary & Outlook

In summary, we have shown that high-efficiency water splitting systems require tandem absorbers specifically adapted to the necessary boundary conditions such as catalysis and cell design. With their flexible optical and electronic properties, combined with mature manufacturing technology, the III-V semiconductors allow for the implementation of highly efficient photoelectrochemical systems. Current work is dedicated to pushing experimental demonstrations further towards the theoretical limits. Depending on the system, this requires a conversion of surplus voltage to current by shifting bandgap combinations, a reduction of reflective losses or photovoltage losses related to energetics and recombination, or – in most cases – a combination of all of them.

Efforts in light concentrating cells, heteroepitaxy of thin-film III-V on Si substrates or inverted metamorphic growth with substrate reuse have the potential to significantly reduce the impact of absorber costs on the overall solar hydrogen price. Also wafer bonding – combined with substrate lift-off – is another emerging technique to remove the restriction of lattice constant-matching or the need for grading layers and therefore promises to benefit efficiencies due to an enhanced flexibility. Yet even if other absorber systems turn out to be more cost-competitive, the III-V systems currently serve as a testbed for high-efficiency water splitting in general, with lessons to be learned for catalyst requirements, cell design, and efficiency validation.

## Acknowledgements

MMM acknowledges funding from the fellowship programme of the German National Academy of Sciences Leopoldina, grant LPDS 2015-09. HD acknowledges support by an EU Marie Curie Fellowship (IOF no. 300971). JAT acknowledges support from the U.S. Department of Energy, Office of Science, Office of Basic Energy Sciences, Solar Photochemistry Program under Contract Number DE-AC36-08GO28308.

## References

1. Bard, A. J. & Fox, M. A. *Acc. Chem. Res.* **28**, 141–145 (1995).
2. Pinaud, B. A. *et al. Energy Environ. Sci.* **6**, 1983–2002 (2013).
3. Austin, I. & Mott, N. *Adv. Phys.* **18**, 41–102 (1969).
4. Nakamura, A., Ota, Y., Koike, K., Hidaka, Y., Nishioka, K., Sugiyama, M. & Fujii, K. *Appl. Phys Express* **8**, 107101 (2015).
5. Ohlmann, J., Sanchez, J. F. M., Lackner, D., Förster, P., Steiner, M., Fallisch, A. & Dimroth, F. *AIP Conf. Proc.* **1766**, 080004 (2016).
6. Nielander, A. C., Shaner, M. R., Papadantonakis, K. M., Francis, S. A. & Lewis, N. S. *Energy Environ. Sci.* **8**, 16–25 (2015).
7. Hannappel, T., May, M. M. & Lewerenz, H.-J. in *Photoelectrochemical Water Splitting: Materials, Processes and Architectures* (eds Lewerenz, H.-J. & Peter, L.) 223–265 (The Royal Society of Chemistry, 2013).
8. Kaiser, B., Fertig, D., Ziegler, J., Klett, J., Hoch, S. & Jaegermann, W. *ChemPhysChem* **13**, 3053–3060 (2012).
9. Zhong, D. K., Choi, S. & Gamelin, D. R. *J. Am. Chem. Soc.* **133**, 18370–18377 (2011).
10. Vurgaftman, I., Meyer, J. R. & Ram-Mohan, L. R. *J. Appl. Phys.* **89**, 5815–5875 (2001).
11. Shockley, W. & Queisser, H. J. *J. Appl. Phys.* **32**, 510–519 (1961).
12. Baruch, P., Vos, A. D., Landsberg, P. & Parrott, J. *Sol. Energy Mater. Sol. Cells* **36**, 201–222 (1995).
13. Yan, Y., Crisp, R. W., Gu, J., Chernomordik, B. D., Pach, G. F., Marshall, A. R., Turner, J. A. & Beard, M. C. *Nat. Energy* **2**, 17052 (2017).
14. Winkler, M. T., Cox, C. R., Nocera, D. G. & Buonassisi, T. *Proc. Natl. Acad. Sci. U.S.A.* **110**, E1076–E1082 (2013).
15. May, M. M., Lackner, D., Ohlmann, J., Dimroth, F., van de Krol, R., Hannappel, T. & Schwarzburg, K. *Sustainable Energy & Fuels* **1**, 492–503 (2017).
16. Bard, A. J. & Faulkner, L. R. 2nd ed. (Wiley, New York, 2001).
17. Koper, M. T. *J. Electroanal. Chem.* **660**, 254–260 (2011).
18. McCrory, C. C. L., Jung, S., Ferrer, I. M., Chatman, S. M., Peters, J. C. & Jaramillo, T. F. *J. Am. Chem. Soc.* **137**, 4347–4357 (2015).
19. Schreier, M., Héroguel, F., Steier, L., Ahmad, S., Luterbacher, J. S., Mayer, M. T., Luo, J. & Grätzel, M. *Nat. Energy* **2**, 17087 (2017).
20. Parkinson, B. & Turner, J. in *Photoelectrochemical Water Splitting: Materials, Processes and Architectures* (eds Lewerenz, H.-J. & Peter, L.) 1–18 (The Royal Society of Chemistry, 2013).
21. Azarpira, A. *et al. Adv. Energy Mater.* **5**, 1402148 (2015).
22. Parkinson, B. *Acc. Chem. Res.* **17**, 431–437 (1984).
23. Murphy, A., Barnes, P., Randeniya, L., Plumb, I., Grey, I., Horne, M. & Glasscock, J. *Int. J. Hydrogen Energy* **31**, 1999–2017 (2006).

24. Döscher, H., Geisz, J. F., Deutsch, T. G. & Turner, J. A. *Energy Environ. Sci.* **7**, 2951–2956 (2014).
25. Degani, Y., Sheng, T., Heller, A., Aspnes, D., Studna, A. & Porter, J. *J. Electroanal. Chem. Interfacial Electrochem.* **228**, 167–178 (1987).
26. Kou, L., Labrie, D. & Chylek, P. *Appl. Opt.* **32**, 3531–3540 (1993).
27. Dohrmann, J. K. & Schaaf, N.-S. *J. Phys. Chem.* **96**, 4558–4563 (1992).
28. Walczak, K. *et al. ChemSusChem* **8**, 544–551 (2015).
29. Murakami, M. & Koide, Y. *Crit. Rev. Solid State Mater. Sci.* **23**, 1–60 (1998).
30. Singh, M. R., Xiang, C. & Lewis, N. S. *Sustainable Energy & Fuels* **1**, 458–466 (2017).
31. Seitz, L. C., Chen, Z., Forman, A. J., Pinaud, B. A., Benck, J. D. & Jaramillo, T. F. *ChemSusChem* **7**, 1372–1385 (2014).
32. Fountaine, K. T., Lewerenz, H. J. & Atwater, H. A. *Nat. Commun.* **7**, 13706 (2016).
33. Forbes, L. *Solid-State Electron.* **18**, 635–640 (1975).
34. Peter, L. M. & Uppul Wijayantha, K. G. *ChemPhysChem* **15**, 1983–1995 (2014).
35. Barroso, M., Pendlebury, S. R., Cowan, A. J. & Durrant, J. R. *Chem. Sci.* **4**, 2724–2734 (2013).
36. Almosni, S. *et al. J. Appl. Phys.* **113**, 123509 (2013).
37. Cariou, R. *et al. IEEE J. Photovolt.* **7**, 367–373 (2017).
38. Döscher, H., Kunert, B., Beyer, A., Supplie, O., Volz, K., Stolz, W. & Hannappel, T. *J. Vac. Sci. Technol., B: Microelectron. Nanometer Struct.* **28**, C5H1 (2010).
39. Romanyuk, O., Supplie, O., Susi, T., May, M. M. & Hannappel, T. *Phys. Rev. B* **94**, 155309 (2016).
40. Wood, B. C., Schwegler, E., Choi, W. I. & Ogitsu, T. *J. Phys. Chem. C* **118**, 1062–1070 (2014).
41. May, M. M., Lewerenz, H.-J. & Hannappel, T. *J. Phys. Chem. C* **118**, 19032–19041 (2014).
42. Young, J. L., Döscher, H., Turner, J. A. & Deutsch, T. G. *J. Phys. Chem. C* **120**, 4418–4422 (2016).
43. May, M. M., Lewerenz, H.-J., Lackner, D., Dimroth, F. & Hannappel, T. *Nat. Commun.* **6**, 8286 (2015).
44. Calvet, W., Murugasen, E., Klett, J., Kaiser, B., Jaegermann, W., Finger, F., Hoch, S., Blug, M. & Busse, J. *Phys. Chem. Chem. Phys.* **16**, 12043–12050 (2014).
45. Young, J. L., Steiner, M. A., Döscher, H., France, R. M., Turner, J. A. & Deutsch, T. G. *Nat. Energy* **2**, 17028 (2017).
46. Sagol, B. E., Seidel, U., Szabó, N., Schwarzburg, K. & Hannappel, T. *Chimia* **61**, 775–779 (2007).
47. Meng, A. C., Cheng, J. & Sprik, M. *J. Phys. Chem. B* **120**, 1928–1939 (2016).
48. Pham, T. A., Ping, Y. & Galli, G. *Nat. Mater.* **16**, 401–408 (2017).

49. Létay, G. and Bett, A. W. *Proceedings of the 17th European Photovoltaic Solar Energy Conference*, 178–181 (2001).
50. Green, M. A. *Prog. Photovolt: Res. Appl.* **20**, 472–476 (2012).
51. Hernández, S., Barbero, G., Saracco, G. & Alexe-Ionescu, A. L. *J. Phys. Chem. C* **119**, 9916–9925 (2015).
52. Khaselev, O. & Turner, J. A. *Science* **280**, 425–427 (1998).
53. Sheng, X. *et al.* in *2014 IEEE Photonics Conference* (2014), 433–434.
54. Weber, M. & Dignam, M. *Int. J. Hydrogen Energy* **11**, 225–232 (1986).
55. Welker, H. *Physica* **20**, 893–909 (1954).
56. Chapin, D. M., Fuller, C. S. & Pearson, G. L. *J. Appl. Phys.* **25**, 676–677 (1954).
57. Gremmelmaier, R. English. *Z. Naturforsch., A: Phys. Sci.* **10**, 501–502 (1955).
58. Loferski, J. J. *J. Appl. Phys.* **27**, 777–784 (1956).
59. Alferov, Z., Andreev, V., Kagan, M., Protasov, I. & Trofim, V. *Soviet physics. Semiconductors* **4**, 2047–2048 (1971).
60. James, L. W. & Moon, R. L. *Appl. Phys. Lett.* **26**, 467–470 (1975).
61. Yoneyama, H., Sakamoto, H. & Tamura, H. *Electrochim. Acta* **20**, 341–345 (1975).
62. Bedair, S. M., Lamorte, M. F. & Hauser, J. R. *Appl. Phys. Lett.* **34**, 38–39 (1979).
63. Knechtli, R. C., Loo, R. Y. & Kamath, G. S. *IEEE Trans. Electron Devices* **31**, 577–588 (1984).
64. Flores, C., Campesato, R., Paletta, F., Timo, G. L., Rossi, E., Brambilla, L., Caon, A., Contini, R. & Svelto, F. in *Conference Record of the Twenty Third IEEE Photovoltaic Specialists Conference* (1993), 1369–1374.
65. Strobl, G. F. X., Ebel, L., Fuhrmann, D., Guter, W., Kern, R., Khorenko, V., Koestler, W. & Meusel, M. in *Conference Record of the 40th IEEE Photovoltaic Specialists Conference* (2014), 3595–3600.
66. Horowitz, K. A. W., Woodhouse, M., Lee, H. & Smestad, G. P. *AIP Conf. Proc.* **1679**, 100001 (2015).
67. Press Release, Fraunhofer ISE (Dec. 2014).
68. Heller, A., Aharon-Shalom, E., Bonner, W. A. & Miller, B. *J. Am. Chem. Soc.* **104**, 6942–6948 (1982).
69. Verlage, E., Hu, S., Liu, R., Jones, R. J. R., Sun, K., Xiang, C., Lewis, N. S. & Atwater, H. A. *Energy Environ. Sci.* **8**, 3166–3172 (2015).
70. Khaselev, O., Bansal, A. & Turner, J. *Int. J. Hydrogen Energy* **26**, 127–132 (2001).
71. Licht, S., Wang, B., Mukerji, S., Soga, T., Umeno, M. & Tributsch, H. *Int. J. Hydrogen Energy* **26**, 653–659 (2001).
72. Jia, J., Seitz, L. C., Benck, J. D., Huo, Y., Chen, Y., Ng, J. W. D., Bilir, T., Harris, J. S. & Jaramillo, T. F. *Nat. Commun.* **7**, 13237 (2016).
73. Nozik, A. J. *Appl. Phys. Lett.* **29**, 150–153 (1976).
74. Kainthla, R. C., Zelenay, B. & Bockris, J. O. *J. Electrochem. Soc.* **134**, 841–845 (1987).

75. Bertness, K. A., Kurtz, S. R., Friedman, D. J., Kibbler, A. E., Kramer, C. & Olson, J. M. *Appl. Phys. Lett.* **65**, 989–991 (1994).
76. Dimroth, F., Beckert, R., Meusel, M., Schubert, U. & Bett, A. W. en. *Prog. Photovolt: Res. Appl.* **9**, 165–178 (2001).
77. Muñoz, A. G., Heine, C., Lublow, M., Klemm, H. W., Szabó, N., Hannappel, T. & Lewerenz, H.-J. *ECS J. Solid State Sci. Technol.* **2**, Q51–Q58 (2013).
78. Porter, J. D., Heller, A. & Aspnes, D. E. *Nature* **313**, 664–666 (1985).
79. Cheng, W.-H., Richter, M. H., May, M. M., Ohlmann, J., Lackner, D., Dimroth, F., Hannappel, T., Atwater, H. A. & Lewerenz, H.-J. *arXiv:1706.01493* (2017).
80. Döscher, H., Young, J. L., Geisz, J., Turner, J. & Deutsch, T. *Energy Environ. Sci.* **9**, 74–80 (2016).
81. Geisz, J. F. *et al. Appl. Phys. Lett.* **91**, 023502 (2007).
82. NREL Efficiency Chart. <https://www.nrel.gov/pv> (2017).
83. Steiner, M. A., Geisz, J. F., García, I., Friedman, D. J., Duda, A. & Kurtz, S. R. *J. Appl. Phys.* **113**, 123109 (2013).
84. Shahrjerdi, D. *et al. Appl. Phys. Lett.* **100**, 053901 (2012).
85. Smeenk, N. J., Engel, J., Mulder, P., Bauhuis, G. J., Bissels, G. M. M. W., Schermer, J. J., Vlieg, E. & Kelly, J. J. *ECS J. Solid State Sci. Technol.* **2**, P58–P65 (2013).
86. Woodhouse, M. & Goodrich, A. Tech. rep. (NREL, 2013).
87. Bansal, A. & Turner, J. A. *J. Phys. Chem. B* **104**, 6591–6598 (2000).
88. Bolton, J. R., Strickler, S. J. & Connolly, J. S. *Nature* **316**, 495–500 (1985).
89. Boettcher, S. W. *et al. J. Am. Chem. Soc.* **133**. PMID: 21214239, 1216–1219 (2011).
90. Jain, N. *et al. in Conference Record of the 43rd IEEE Photovoltaic Specialists Conference* (2016), 0046–0051.
91. NREL-SRRL. <https://www.nrel.gov/midc/srml.bms>.
92. ASTM, G. *West Conshohocken, PA: ASTM International* (2003).
93. Cannon, T. *Solar Cells* **18**, 233–241 (1986).
94. Furtak, T. E., Canfield, D. C. & Parkinson, B. A. *J. Appl. Phys.* **51**, 6018–6021 (1980).
95. Snaith, H. J. *Energy Environ. Sci.* **5**, 6513–6520 (2012).
96. Siefert, G., Baur, C., Meusel, M., Dimroth, F., Bett, A. W. & Warta, W. in *Conference Record of the Twenty-Ninth IEEE Photovoltaic Specialists Conference* (2002), 836–839.
97. Baur, C. & Bett, A. W. in *Conference Record of the Thirty-First IEEE Photovoltaic Specialists Conference* (2005), 583–586.
98. Metzendorf, J. *Appl. Opt.* **26**, 1701–1708 (1987).
99. Winter, S., Fey, T., Kröger, I., Friedrich, D., Ladner, K., Ortel, B., Pendsa, S. & Witt, F. *Measurement* **51**, 457–463 (2014).